Materials Advances

ROYAL SOCIETY OF CHEMISTRY

PAPER

View Article Online
View Journal | View Issue

Cite this: *Mater. Adv.*, 2026, 7, 2937

Optimization of diffusion dynamics in Mn-doped Co_3O_4/rGO hybrid electrodes for efficient energy storage in asymmetric supercapacitors

Farhan Ahmad,[a] Abdul Shakoor,[a] Ahsan Iqbal,[a] Asif Mahmood,[b] Waheed Al-Masry,[b] Farooq Ahmad[a] and Shahid Atiq*[a]

Efficient electrode materials are crucial to meet the growing modern-day energy storage needs. In this context, a series of electrodes composed of Co_3O_4 with varying levels of Mn doping (4% and 8%) and varying rGO contents (4% and 8%) were prepared using a combination of hydrothermal and solvothermal methods. The samples were labeled as Co_3O_4 (CoO), $Co_{2.96}Mn_{0.04}O_4$ (MDCoO-I), $Co_{2.92}Mn_{0.08}O_4$ (MDCoO-II), $Co_{2.92}Mn_{0.08}O_4$@4%rGO (MDCoO-III), and $Co_{2.92}Mn_{0.08}O_4$@8%rGO (MDCoO-IV). Various tests confirmed the formation of the desired phase, with X-ray diffraction showing a cubic structure that remained consistent throughout the series. Following this survey, comprehensive electrochemical testing of all samples was conducted in a three-electrode setup to identify the best candidate for practical device applications. For example, MDCoO-IV showed enhanced ion transport properties, including ion conductivity (0.62 S cm^{-1}), transference number (0.45), rate constant (2.21 × 10^{-7} cm s^{-1}), exchange current density (0.021 A g^{-1}), and a notable value of diffusion coefficient (5.51 × 10^{-13} m^2 s^{-1}), due to efficient coupling of conduction mechanism facilitated by 8% rGO inclusion across the pseudocapacitive enriched surface-active chemistry of $Co_{2.92}Mn_{0.08}O_4$. Owing to the efficient ion-transport characteristics, an asymmetric assembly with full device testing using MDCoO-IV was subsequently established, demonstrating good rate performance with a specific capacitance of about 833.25 F g^{-1} and an energy density of 57.86 Wh kg^{-1} at 1250 W kg^{-1}, thereby maintaining 87.27% after 10 000 cycles. The discovery of these features suggests that this material has potential for use in future energy storage devices.

Received 14th July 2025,
Accepted 7th January 2026

DOI: 10.1039/d5ma00752f

rsc.li/materials-advances

1. Introduction

The relentless depletion of natural reservoirs due to eruptive population growth has led to severe environmental pollution and various consequential threats to human survival. Several scientific surveys have demonstrated that conventional reservoirs face multiple issues, including unavailability and depletion over time.[1,2] In this context, introducing energy resources that can mitigate these challenges has become an urgent need for the scientific community to address. Therefore, sustainable energy technology presents an excellent alternative to tackle these problems by bridging the gap between energy consumption and production, paving the way for environmental friendliness through various energy storage devices.[3,4] Hence, rechargeable batteries and supercapacitors (SCs) have attracted considerable attention due to their numerous features, which depend on the specific application. SCs within this context are regarded as unique candidates among various energy storage devices, distinguished by their excellent power density (PD), admirable cycle life, high coulombic efficiency, fast charge/discharge rate, and lightweight design.[5–11]

Therefore, research is being conducted to enhance the performance of SCs through the discovery of novel electrode materials. Generally, SCs are classified into two groups based on their charge storage processes: pseudo and electric double-layer capacitors (EDLCs). Both types significantly depend on the nature of the electrode material and electrolyte used, influencing the performance parameters (ED, PD, *etc.*) of the device.[12] For instance, in pseudocapacitors (PCs), charges are stored through the electrochemical intercalation and deintercalation of ions, while in EDLCs, the electrostatic adsorption and desorption of ions are involved. Moreover, different varieties of carbon-based materials are employed in EDLCs primarily owing to their unique non-faradaic characteristics. In contrast, PCs promote the use of transition metal oxides (TMOs) and conducting polymers, facilitating redox activities.[13] The charge storage performance of SCs is significantly influenced by the active sites, which are directly

[a] *Centre of Excellence in Solid State Physics, University of the Punjab, Lahore-54590, Pakistan. E-mail: satiq.cssp@pu.edu.pk*
[b] *College of Engineering, Chemical Engineering Department, King Saud University, 11421, Riyadh, Saudi Arabia*

correlated with the material's morphological properties and surface chemistry, as well as electrode–electrolyte interactions.[14] EDLCs offer higher PD and a good cyclic lifetime, but have limited energy density (ED). In contrast, PCs offer higher specific capacitance (C_{sp}) and ED based on their outstanding reversibility, minimal PD, and rate capabilities. The core challenge is identifying materials that can enhance the energy storage of SCs without compromising the PD.[15]

Moreover, the performance, which significantly depends on the charge storage capacity of SCs, is greatly influenced by the nature of the electrode material. Consequently, researchers are focused on identifying new electrode materials with superior properties. In this context, TMOs have attracted substantial research attention worldwide due to their greater abundance compared to other 2D materials.[16,17] Within this framework, researchers have explored various composites of TMOs with enhanced ion transport attributes through different treatments, such as doping and substitution, along with hybrid technologies, to achieve balanced results.[16] Primarily, the scientific community has studied TMOs, including TiO_2, RuO_2, Mn_3O_4, NiO, Fe_3O_4, Co_3O_4 (CoO), V_2O_5, and MoO_3, to evaluate their potential for SCs, which have gained significant research interest in recent years because of their remarkable structural stability and ability to exist in multiple oxidation states.[18–23] These characteristics position these materials as promising candidates for SC applications. Notably, CoO has been widely researched in recent years owing to its high theoretical capacitance of $\sim$3560 F g^{-1}, low cost and natural abundance, exceptional environmental friendliness, and well-characterized redox properties compared to many other TMOs.

Numerous reports have been published on the enhanced rate performance of transition metal-doped CoO as an electrode material for SCs. For instance, Alem *et al.* reported Ag–CoO nanoparticles synthesized through the coprecipitation synthesis route, which offered a C_{sp} of 992.7 F g^{-1} at 5 mV s^{-1}, along with ED and PD values of 27.9 Wh kg^{-1} and 3816.1 W kg^{-1}, respectively.[20] In another work, Deng *et al.* developed Cd-doped CoO nanosheets using the same synthesis route, which resulted in a C_{sp} of 737 F g^{-1} at a current density (I_m) of 1 A g^{-1}.[21] Furthermore, Chen *et al.* developed Mn-doped CoO *via* a solvothermal approach, yielding a C_{sp} of 909 F g^{-1} at 1 A g^{-1}.[22] Karthikeyan *et al.* employed a coprecipitation method to prepare Mn-doped CoO nanomaterials, achieving a C_{sp} of 625 F g^{-1} at a I_m of 1.5 A g^{-1}. The retention over 1500 cycles was 96%.[23] In another research study, using a similar synthesis technique, they synthesized Ni-doped CoO nanoparticles, which exhibited a C_{sp} of 347 F g^{-1} at 1.5 A g^{-1} and retained a superior capacity of 90% after 5k cycles.[24] Based on the insightful findings of Mn-doped CoO based reports, Wang *et al.* developed nanowires of Mn-doped CoO (Mn-doped Co_3O_4) with a 1 : 5 ratio and constructed an asymmetric device, which delivered the maximum C_{sp} (105.80 F g^{-1}), ED (33 Wh kg^{-1}), and PD (748.10 W kg^{-1}) with storage retention of about 60.20%.[25] On the other hand, Rabecca *et al.* reported a triphasic composite of CoO with Mn_2O_3/rGO, which delivered the highest C_{sp} of about 663 F g^{-1}/.[26]

To further enhance the performance of SCs, researchers are currently developing electrodes made from carbonaceous materials, such as reduced graphene oxide (rGO). The literature also indicates that incorporating rGO can improve the C_{sp} of transition metal-doped TMOs due to a significant increase in specific surface area (SSA) through the formation of porous networks. This effect is achieved by enhancing electrical conductivity, which facilitates the transportation of ions and charges, thereby resulting in improved ED and PD. The effectiveness of an electrode relies not only on the composition of the material but also on other parameters, such as crystallinity, particle size, morphology, and structural stability. Because several material properties are interrelated, improving one may compromise another. Notably, adding rGO to any species increases the number of reaction sites while decreasing material crystallinity. In addition to this, the choice of the synthesis route has a significant influence on such attributes. In this regard, various methods have been utilized, including solid-state, sol–gel, and solvothermal methods. However, in the current study, we preferred the hydrothermal and solvothermal synthesis routes because particle growth and morphology are significantly controlled through these routes, allowing for constant temperature and high pressure, which yields promising results.

In this context, the significance of the present work lies in improving the electrochemical properties of CoO (Co_3O_4) by incorporating optimal doping concentrations of Mn and rGO under specific conditions *via* the hydrothermal and solvothermal synthesis routes. The prime characteristics, in principle, are offered by Mn, as Mn-doping induces oxygen vacancies in the cubic lattice of CoO due to charge compensation between Mn and Co ions. These defects serve as active sites for redox reactions, aiding in the adsorption and diffusion of electrolyte ions, which are crucial for enhancing the pseudocapacitive behavior of SCs. So, Mn-doping not only enhances oxidation flexibility but also preserves the structural and electronic stability during repeated charge–discharge cycles. Consequently, our research group has identified optimal concentrations of Mn to enhance CoO's electrochemical performance by developing efficient electrode materials for high-performance energy storage systems, all without altering the crystal structure. Furthermore, to accelerate the conduction mechanism in redox-active channels, Mn-doped CoO has been combined with two optimal weight percentages of rGO. In a nutshell, the prime objectives of this study were to control ion accumulation within the redox-active channels of CoO and to prevent structural degradation during repeated charge/discharge cycles through Mn-doping and inclusion of specific weight percentages of rGO.

As described, the roadmap of this research work is based on experimental evidence showing how optimal levels of the Mn dopant and rGO improve electrochemical performance in efficient energy storage devices. For instance, evaluation of ion transport features in a 3-electrode setup allows for the careful identification of the best composition among the fabricated electrode series for device applications. At this instance, $Co_{2.92}Mn_{0.08}O_4$@8%rGO appears to be the best candidate among all, and its diffusion dynamics at different electrolyte concentrations were studied using the galvanostatic intermittent titration

technique (GITT) in a two-electrode setup. The proposed asymmetric device exhibited excellent energy storage capabilities.

2. Synthesis and electrode fabrication

2.1. Raw materials

All chemical reagents used in the material preparation were acquired from Sigma-Aldrich. The substances used to synthesize the target materials were cobalt nitrate hexahydrate, manganese nitrate hexahydrate, ethanol, rGO, and potassium hydroxide. The electrodes were prepared by combining certain ratios of dimethyl formamide (DMF), polyvinylidene difluoride (PVDF), activated carbon, and the material under investigation. Deionized water (DIW) was used as the solvent all over the process.

2.2. Synthesis of Co_3O_4 (CoO) and Mn-doped Co_3O_4 (MDCoO-I, MDCoO-II)

A hydrothermal material preparation route was used to synthesize both Co_3O_4 (CoO) and Mn-doped Co_3O_4 (MDCoO-I and MDCoO-II with Mn contents of 0.04 and 0.08 molar, respectively). Initially, CoO was produced by dissolving the weighed amount of cobalt nitrate precursors in DIW and stirring for an hour. This solution was transferred to a Teflon-lined stainless-steel autoclave and subjected to heat treatment for 4 h at 170 °C. The final product, after washing, drying, and calcining at 550 °C for 2 h, was ground until it yielded a fine powder. Mn-doped CoO was prepared using stoichiometrically weighed amounts of Mn-nitrates, with molar ratios of 0.04 and 0.08, which were separately mixed with 2.96 and 2.92 molar ratios of Co-nitrate in two beakers containing 40 mL of DIW. The prepared solutions were stirred for 30 min, maintaining a pH of 11 by adding a few drops of KOH solution. Then, these were poured into a Teflon cylinder and heated at 170 °C for 4 h to ensure controlled morphology and homogeneous incorporation of Mn into the CoO lattice. After the reaction was completed, the cylinders were allowed to cool, and the solutions were washed with DIW and ethanol to remove impurities (undesired ionic species). Subsequently, the solutions were dried on a hot plate for 6 h at 40 °C until all solvents had evaporated. To prevent agglomeration and maintain a uniform particle size, the washed and dried materials were ground for 30 min. Finally, the black powders of CoO, MDCoO-I, and MDCoO-II were calcined at 550 °C for 2 h in a muffle furnace, following the same route and conditions.

2.3. Preparation of Mn-doped Co_3O_4/rGO

A series of Mn-doped CoO/rGO (MDCoO-III and MDCoO-IV) nanostructures with two weight percentages of rGO (4 and 8%) were synthesized using the solvothermal route.[41] Stoichiometrically weighed amounts of rGO and Mn-doped CoO were dissolved in 30 mL of ethanol to form a solution. This solution was then sonicated for 1 h and stirred at 250 rpm for 2 h to create a homogeneous solution. Finally, it was carefully transferred into a Teflon cylinder and placed inside the furnace, where it was heated to 170 °C for 4 h. The samples were washed several times in a centrifugation machine to ensure purity after removing contaminants. The developed nanostructures were used as active materials for electrode fabrication.

2.4. Electrode fabrication

Nickel foam (NF) was cut into 1 × 1 cm^2 pieces to serve as a substrate, and was subjected to etching to enhance adhesion through its porous network. These pieces were etched in 50 mL of an acidic medium, such as HCl and DIW, and sonicated for 1 h. After successfully etching the substrate, the binder was prepared by dissolving 0.004 mg of PVDF in 0.08 mL of DMF. Next, the binder, along with the active material (0.034 g) and activated carbon (0.002 g), was stirred in a fixed ratio (10 : 85 : 5) for 8 h to obtain a homogeneous paste, commonly referred to as 4 mg slurry. This mixture was then coated onto the NF to prepare the working electrode. The loading mass on each electrode was measured to be 2 mg. Fig. 1 shows a pictorial representation of sample synthesis and the complete fabrication process of the electrodes.

2.5. Characterization

Structural confirmation of CoO, MDCoO-I, MDCoO-II, MDCoO-III, and MDCoO-IV was conducted using a Bruker D8 advanced X-ray diffractometer with X-rays generated from a Cu-K_α source at a wavelength of 1.54 Å. To examine the surface characteristics and elemental composition of the synthesized materials, we utilized a Nova Nano SEM field-emission electron microscope (FESEM) equipped with an Oxford Analyzer and an energy-dispersive X-ray analysis (EDX) system. Ultimately, the electrochemical characteristics (CV, GCD, and EIS) of the synthesized electrodes were assessed in a 3-electrode system comprising a reference (Ag/AgCl) and a counter (Pt wire) electrode, and a 2 M KOH electrolyte using Corrtest electrochemical & Corrosion Studio (Version 6.4). A cyclic retention study and diffusion dynamics study by GITT were carried out using a two-electrode setup (the selected electrode material and activated carbon as the electrode) along with an asymmetric setup in a 6 M KOH electrolyte for MDCoO-IV to construct and assess the device's efficiency.

3. Results and discussion

3.1. Structural analysis

The XRD patterns of CoO, MDCoO-I, MDCoO-II, MDCoO-III, and MDCoO-IV are shown in Fig. 2(a), aiming to discover their crystalline phase within the 2θ range of 15 to 70°. The methodology proposed by BD Cullity was used to identify and index these patterns.[27] The major peaks were observed at 2θ = 19.09°, 31.36°, 36.84°, 38.58°, 44.95°, 59.39°, and 65.42°, corresponding to the respective values of *hkl* of (111), (220), (311), (222), (400), (511), and (440), which showed a good match with the ICSD reference code 01-073-1701 confirming the cubic spinel structure of CoO (Co_3O_4) with the space group of $Fd\bar{3}m$. Additionally, the standard diffraction pattern has also been provided at the bottom of Fig. 2(a). The absence of the characteristic peak (002) of rGO in the XRD pattern of the MDCoO-IV powder form, which is associated with the inclusion of rGO, reflects the fact that the concentration in the composite samples was too

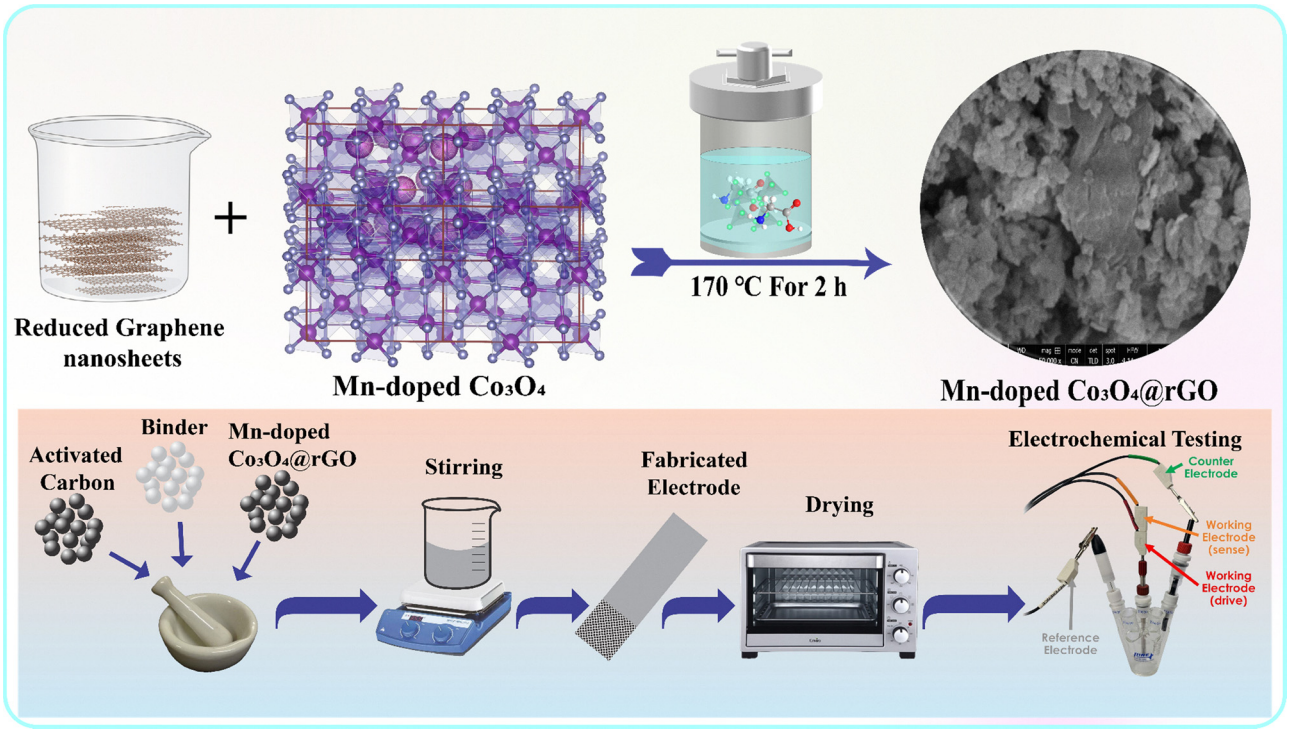

Fig. 1 Synthesis and electrode fabrication profile of all samples.

minute, which diminished the possibility of detecting the characteristic basal planes related to rGO. In the meantime, the XRD patterns of all samples deposited over nickel foam only demonstrated the characteristic peaks of CoO along with three additional peaks at 44.80°, 52.40°, and 76.41° for ICSD # 01-070-0989, implying that Ni existed in these samples, as shown in Fig. S1(a). Moreover, the crystal structure of Co_3O_4 was animated using VESTA software, with identical atomic positions in the unit cell, as displayed in Fig. 2(b). The presence of Ni peaks related to nickel foam and rGO has been verified from the XRD patterns, as displayed in Fig. S1(b). The presence of the purity phase of rGO is reflected in the appearance of a characteristic peak at 26.46°, corresponding to the (002) plane.

The structural fingerprint of CoO, MDCoO-III, and MDCoO-IV was identified through the presence of essential vibrational modes associated with the critical molecules, and has been determined using Raman spectroscopy. From this perspective, in Fig. 2(c), the Raman spectra of CoO and MDCoO-II show the first Raman shift at 191.78 cm^{-1}, representing the first $F_{2g}{}^1$ band. The vibrational bands at the other three peaks have been observed at 477.58, 510.95, and 606.78 cm^{-1}, which are associated with F_g, $F_{2g}{}^2$, and $F_{2g}{}^3$, respectively.[28] The characteristic Raman shift related to the fingerprint of molecules in CoO was also identified at 681.59 cm^{-1}, corresponding to the A_{1g} mode of CoO. These fingerprint regions of CoO (Co_3O_4) have confirmed the presence of essential molecular modes. In addition

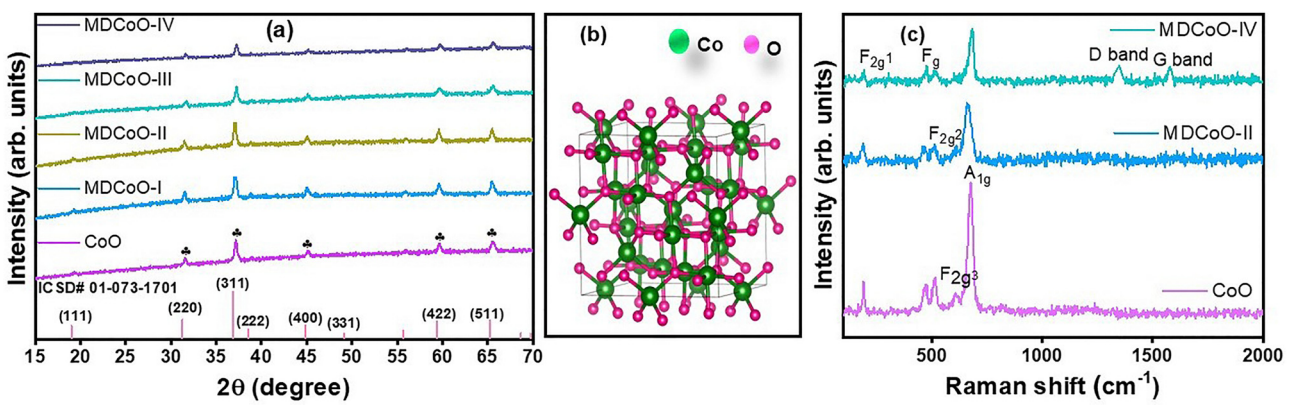

Fig. 2 (a) XRD patterns of CoO, MDCoO-I, MDCoO-II, MDCoO-III, and MDCoO-IV samples, (b) crystal structure of CoO, and (c) Raman spectra of CoO, MDCoO-II, and MDCoO-IV.

to this, the graphitic and disordered bands associated with the presence of rGO were also identified at approximately 1350 and 1581 cm^{-1}, respectively, in the Raman spectra of MDCoO-IV. This is how this survey facilitated the fingerprints of CoO and rGO.

3.2. Morphological and elemental analysis

Fig. 3(a–e) presents the surface features in FESEM images at magnifications of up to 100 000 for CoO, MDCoO-I, MDCoO-II, MDCoO-III, and MDCoO-IV-based samples from a selectively scanned region. This offers clear insights into the morphological characteristics observed under accelerated electrons at a working voltage of 10 kV. The primary goal was to visualize the distribution, shape, and size of grains in a specific region of the sample. For instance, Fig. 3(a) illustrates the highly agglomerated spherical and irregularly shaped grains present. Within this context, Fig. 3(b and c) indicates that the morphology of the spherical particle growth is rapidly influenced by Mn doping, facilitating improved intercalation of the particles.[29–31] Meanwhile, petal-like nanosheets with embedded grains can be observed, exhibiting significant agglomeration, in Fig. 3(b). Such agglomerations have been controlled by adding a dopant concentration at an optimized level, as shown in Fig. 3(c). The corresponding categories of morphological inheritances usually offer a significant improvement in the ion transport attributes due to enhanced active channels.

Furthermore, Fig. 3(d and e) showcases the morphology of the composite form of Mn-doped Co_3O_4 with the inclusion of rGO, varying in weight percentages (4 and 8%). It suggests that the grains are embedded over and around the sheets of rGO, thereby minimizing both the stacking and clustering of nanoparticles, which feature interconnected channels and enhance the conduction mechanism in redox-active channels. This layered structural modification significantly enhances ion mobility, resulting in improved intercalation and facilitating rapid charge transport.[32] The rGO inclusion had a significant effect on the morphology and particle size, as shown in the FESEM images, as displayed in Fig. 3(d and e). The porous structure of the sample enables the faster transfer of electrolyte ions during both charging and discharging stages, making these materials potentially suitable for high-power applications, such as SCs. It can be observed that the rGO nanosheets are obscured due to the minimal concentration used and the excessive growth of nanoparticles over them, which diminishes their visibility and makes them appear less prominent. From this perspective, the FESEM image at 1 μm of pristine rGO is provided in Fig. 3(f) to support the claim of successful incorporation of rGO in the composite samples (MDCoO-III and MDCoO-IV).

EDX analysis is a powerful method for precisely measuring essential elements in a sample and determining their elemental composition by atomic weight percentage. The EDX spectrum shown in Fig. 3(g) exposes the presence and absence of essential and undesired elements in all synthesized recipes. The absence of unusual peaks confirms the successful development of the pure phase. The detected peaks correspond to

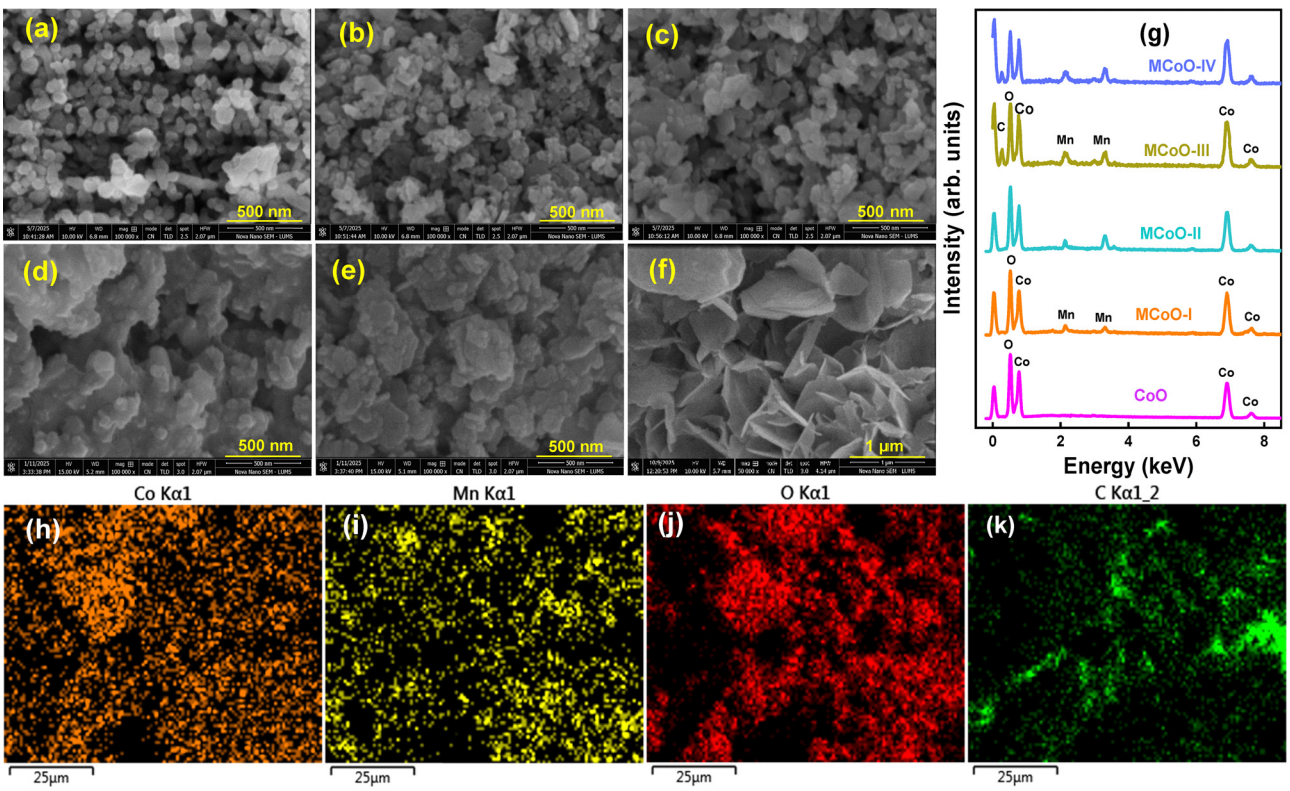

Fig. 3 (a)–(e) FESEM images of CoO, MDCoO-I, MDCoO-II, MDCoO-III, and MDCoO-IV, respectively, at 500 nm, (f) FESEM image of rGO at 1 μm, (g) EDX spectra of all samples, and (h)–(k) elemental mapping images of MDCoO-IV.

Table 1 Elemental composition of CoO, MDCoO-I, MDCoO-II, MDCoO-III, and MDCoO-IV

Sample	wt (%) Co	wt (%) O	wt (%) Mn	wt (%) C
CoO	72.15	21.75	0	6.10
MDCoO-I	69.37	23.95	0.65	6.03
MDCoO-II	63.88	24.35	1.38	6.39
MDCoO-III	60.83	20.96	0.58	17.16
MDCoO-IV	58.43	19.55	1.29	20.73

energy transitions among atoms, indicating the different elements in the composition. Peaks for cobalt, oxygen, and carbon were noted, validating Co as the primary element due to its significant contribution to the elemental makeup, with these peaks attributed to inner K-shell transitions. The oxygen peaks relate to the oxide form of the material, while the C peaks are directly associated with the use of scotch tape to adhere the samples, which functioned as a substrate, and rGO concentration in composite samples.[33–35] The minute inconsistency in these stoichiometric weight percentages is due to the non-uniform yield of electronic transitions, which is affected by the chamber's internal atmosphere. The weight percentages of all the elements present in the specimens are presented in Table 1.

To extend the elemental characterization, elemental mapping of MDCoO-IV was conducted to provide an overview of how each element associated with the sample is distributed. Within this framework, Fig. 3(h–k) reveals the color contrast images related to specific electronic transitions by the corresponding element, where a unique color is used to distinguish each element in $Co_{2.92}Mn_{0.08}O_4$@rGO (MDCoO-IV). For example, Co appeared as fluorescent orange, Mn was neon yellow, O was dark red, and C was lime green in Fig. 3(h–k), respectively. In a nutshell, a uniform distribution of each element has been observed in MDCoO-IV.

3.4. Electrochemical analysis

The potential of CoO, MDCoO-I, MDCoO-II, MDCoO-III, and MDCoO-IV as efficient electrode materials for SC applications was thoroughly investigated using CV analysis in a 1 M KOH electrolyte. Additionally, the understanding of a system's reversibility typically defines its potential, which is estimated from the potential–current response in an electrochemical cell. From this perspective, Fig. 4(a–e) shows the CV curves for the CoO, MDCoO-I, MDCoO-II, MDCoO-III, and MDCoO-IV electrodes within a potential window range of 0–0.50 V for CoO, MDCoO-I, and MDCoO-II, and 0 to 0.55 V for MDCoO-III and MDCoO-IV at diverse scan rates from 5 to 30 mV s^{-1}. It is evident that the CV profiles exhibited a noticeable change from sample to sample, with the diversity of potential/current response, and demonstrated excellent reversibility, even at higher scan rates. This occurs simply with a progressive shift of the oxidation and reduction peaks towards higher and lower potentials, respectively. The development of excessive ion accumulation at the electrode/electrolyte interface, which hinders the balanced neutrality, could be the primary rationale behind the shifting of oxidation towards higher potential segments and reduction towards lower ones. These observations highlight the remarkable stability of the electrode/electrolyte contact, as evident in the CV profiles of all samples.[36]

In a detailed analysis, doping Mn into pristine Co_3O_4 enhances both the reversibility and charge storage capacity, as evident from the potential–current response and the increased area under the CV curve. This observation remains valid even when the doping level of Mn is further elevated, as verified by the range of current responses displayed on the *y*-axis in CV curves. The substantial current response observed in the voltammograms is primarily attributed not only to the charging by EDLCs, which usually appears in the preceding region of the redox peaks, but also to the Mn^{3+}/Mn^{2+} and Mn^{4+}/Mn^{3+} redox transitions. Surface faradaic reactions involve the adsorption of electrolyte ions onto the electrode surface. In contrast, bulk redox processes occur through the intercalation and deintercalation of alkali metal cations within the material's structure.[37]

These chemical transformations exhibit a high degree of reversibility.[38] In principle, cobalt-based oxides show higher electrochemical activity compared to simple manganese-based oxides due to their structural stability. In this context, the electrochemical activity of cobalt oxide can be further improved by incorporating the beneficial redox-active surface chemistry of manganese into its redox channels, up to an optimal doping level. This enhancement promotes the formation of more oxygen vacancies with interesting defects and increases the number of defective sites. This, in turn, improves electrical conductivity, ion diffusion, and structural stability during the expansion and contraction of the lattice caused by oxidation and reduction processes.[30,39] Adding rGO to Mn-doped cobalt oxide further improves reversibility, as demonstrated by the gradual enhancement in the potential–current response seen in Fig. 4(b–e) for MDCoO-I, MDCoO-II, MDCoO-III, and MDCoO-IV, respectively, compared to the potential–current response in Fig. 4(a) from CoO. As a result, doping Mn into cobalt, along with the addition of rGO, substantially increases the Q_s of the electrode material. Such structural integrity facilitates efficient ion transport, allowing both the outer and inner surfaces of the electrode to be accessed at low scan rates. However, ion diffusion becomes restricted at higher scan rates, limiting full utilization of the inner surface area due to kinetic hindrances that dominate surface-controlled processes. This is logistically evident from the preceding region of oxidation and reduction peaks, where we can't observe any current variations in response to increasing potential window. For instance, Fig. S2(a–e) presents the marked points of oxidation and reduction peaks at 5 mV s^{-1} for CoO, MDCoO-I, MDCoO-II, MDCoO-III, and MDCoO-IV, signifying the transitions of Co_3O_4 from Co^{2+} to Co^{3+} during oxidation, and *vice versa* during reduction. Such plateaus are the symbols of faradaic reactions. These are absent in the preceding regions of these peaks and humps, which also appear to be approximately straight lines up to 0.2 V, where no significant current variations can be observed. Development of excessive ion accumulation at the electrode–electrolyte interface is the main factor behind the shifting of oxidation and reduction peaks with scan rate variation toward higher and lower potentials. It can also be deduced that faradaic reactions are always vibrant at lower scan rates and badly influenced at higher scan rates.[40]

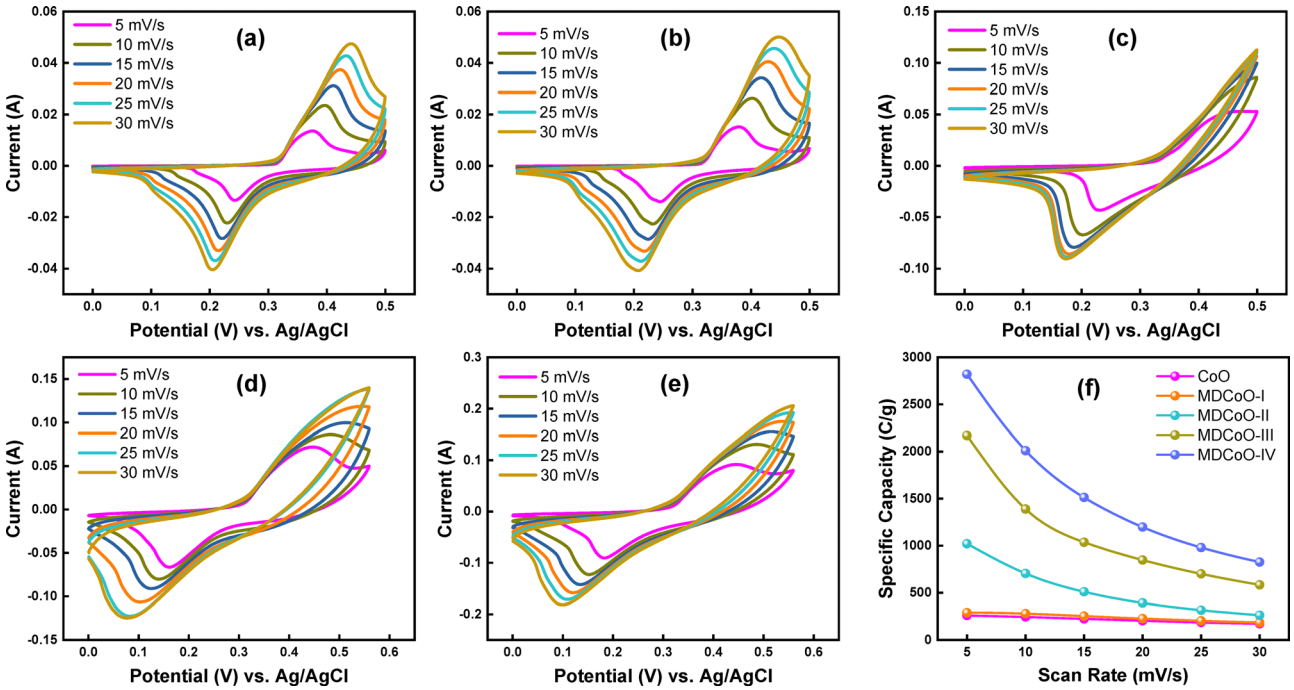

Fig. 4 CV curves at different scan rates for (a) CoO, (b) MDCoO-I, (c) MDCoO-II, (d) MDCoO-III, and (e) MDCoO-IV, and (f) scan rate *vs.* specific capacity.

Additionally, the symmetry observed in the CV curves suggests partial irreversibility within the system. The faradaic redox process exhibits reversible characteristics but the polarization effects prevent complete kinetic optimization of the redox activity and accommodate the non-faradaic charge storage mechanism.[41] In the meantime, a comparative representation of the CV profiles for all samples recorded at the lowest scan rate of 5 mV s^{-1} is shown in Fig. S2(f). Fig. S2(f) provides an explicit insight into how charge storage capacity and reversibility of the as-fabricated electrode series are demonstrated. The specific capacity (Q_s) was determined using eqn (1) due to the combination of both EDLC and pseudocapacitance, originating from non-faradaic and faradaic charge storage mechanisms.[19]

$$Q_s = \frac{\int_{V_a}^{V_b} I(V)\mathrm{d}v}{v \times m} \quad (1)$$

The integral term represents the area under the voltammogram, m is the mass of the active material, v is the scan rate, and (V_a–V_b) corresponds to the potential window. The Q_s values of CoO, MDCoO-I, MDCoO-II, MDCoO-III, and MDCoO-IV across varying scan rates are summarized in Table 2 and visually represented in Fig. 4(f). A distinct decline in the Q_s value was observed with increasing scan rates. At lower scan rates, sufficient time is available for ions to diffuse into the deeper pores of the electrode material in response to the slow electrical signal, enabling the maximum utilization of active sites and resulting in higher Q_s values. Conversely, at higher scan rates, the limited diffusion time hinders ion transport into the bulk material, restricting the electrochemical reaction primarily to the electrode surface and consequently reducing the Q_s value.

To estimate the capacitive and diffusive processes that contribute to the overall pseudocapacitive component in the CV curve, the contributions from the oxidation and reduction peaks at different scan rates in each sample have been analyzed. The positions of these peaks for each sample are highlighted by the dotted circles in Fig. S2(a–e) at 5 mV s^{-1}. In principle, capacitive effects originate from the partially non-faradaic activity of monolayer formation, while diffusive processes reflect the intercalated redox reactions. This has been achieved by employing a mathematical approach developed to investigate the detailed impact of scan rate and material variations on the charge storage processes and the device's overall efficiency. Dunn's model and Cottrell's equations, based on the Power law, as equated in eqn (2) and (3), have been used to analyze these components and were applied to the CV graphs.

$$i_{peak} = av^b \text{ or } \log(i_{peak}) = b\log(v) + \log(a) \quad (2)$$

Table 2 Specific capacities of CoO, MDCoO-I, MDCoO-II, MDCoO-III, and MDCoO-IV at different scan rates

Scan rate (mV s^{-1})	CoO	MDCoO-I	MDCoO-II	MDCoO-III	MDCoO-IV
	Specific capacities (C g^{-1})				
5	260	290	1020	2170	2820
10	245	280	705	1390	2010
15	223	253	510	1036	1513
20	205	227	392	847.5	1197
25	186	204	316	700	980
30	171	185	263	583	825

$$i(v) = k_1 v + k_2 v^{1/2} \quad (3)$$

In electrochemical studies, the b value obtained from Power's law, as stated in eqn (2), can predict the charge storage mechanism of an electrode material. A b-value of 0.5 reflects that the maximum contribution in the charge storage mechanism is due to a diffusion-controlled process, and a b-value of 1 indicates a capacitive process. In contrast, if the value falls between 0.5 and 1 or below 0.5, it will accurately reflect the hybrid transitions, which combine both diffusion-controlled and capacitive process features.[42] Such hybrid behavior shows that the material can store charge *via* both faradaic and partially non-faradaic (due to the redox active mono-layer, which is partially faradaic and becomes non-faradaic in certain circumstances) processes, as shown in Fig. 5(a–e). The combined plot based on the Power law's depiction of all samples is shown in Fig. 5(f).

From eqn (3), $i(v)$ describes the total peak value of current at a given scan rate with two contributions, $k_1\upsilon$ being the capacitive current and $k_2 v^{1/2}$ being the diffusion-controlled, as illustrated in Fig. S3(a–e). This capacitive contribution occurs through the adsorption and desorption processes of ions, resulting in the formation of a monolayer or Helmholtz layers at the electrode interface. The diffusive contribution, on the other hand, arises from the partial development of pseudocapacitive behavior and is associated with faradaic reactions. Based on this analysis, the proportions of capacitive (surface-controlled) and diffusive (bulk-controlled) processes concerning scan rate are shown in Fig. 6(a–e). Additionally, the accuracy of these processes at lower scan rates is demonstrated in Fig. 6(f) for all electrodes. Moreover, these are also illustrated in the CV curves at individual scan rates for all samples in Fig. S4–S8. It can be observed from various depictions that as the scan rate increases, capacitive behavior increases while diffusive behavior decreases; the reason for this is the type of storage mechanism involved in partially non-faradaic and faradaic reactions, respectively. For instance, Fig. 6(a–e) illustrates the combined capacitive and diffusive contributions of samples at different scan rates, revealing the overall charge storage mechanism. At a lower scan rate for all samples (v = 5 mV s^{-1}), approximately 65, 89, 7, 80, and 40% of the total charge storage is due to diffusion-controlled contributions, and 35, 11, 93, 20, and 60% is due to capacitive contributions. The prevalence of diffusion-controlled processes at lower scan rates is generally associated with the complete diffusion of ions in the electrolyte to the electrode surface. For all samples, as the scan rate increases, the capacitive contribution increases to 56, 22, 97, 38, and 79% at v = 30 mV s^{-1}, while the diffusion-controlled contribution decreases to 21%. These transitions suggest that as the scan rate increases, the short time available for ion diffusion during the rapid charge–discharge process favors capacitive processes. At higher scan rates, capacitive behavior predominates due to the electrochemical response of electrode materials compared to the slower diffusion of ions.

GCD measurements were conducted at multiple I_m to investigate the charge storage capacity and assess the performance of CoO, MDCoO-I, MDCoO-II, MDCoO-III, and MDCoO-IV for SC applications. The GCD curves presented in Fig. 7(a–e) display a non-linear charge–discharge profile across different I_m (2.5 to 20 A g^{-1}) within a fixed potential range of 0.0–0.5 V for CoO and MDCoO-I and 0 to 0.4 V for all other samples. This non-linearity can be attributed to rapid redox reactions, as

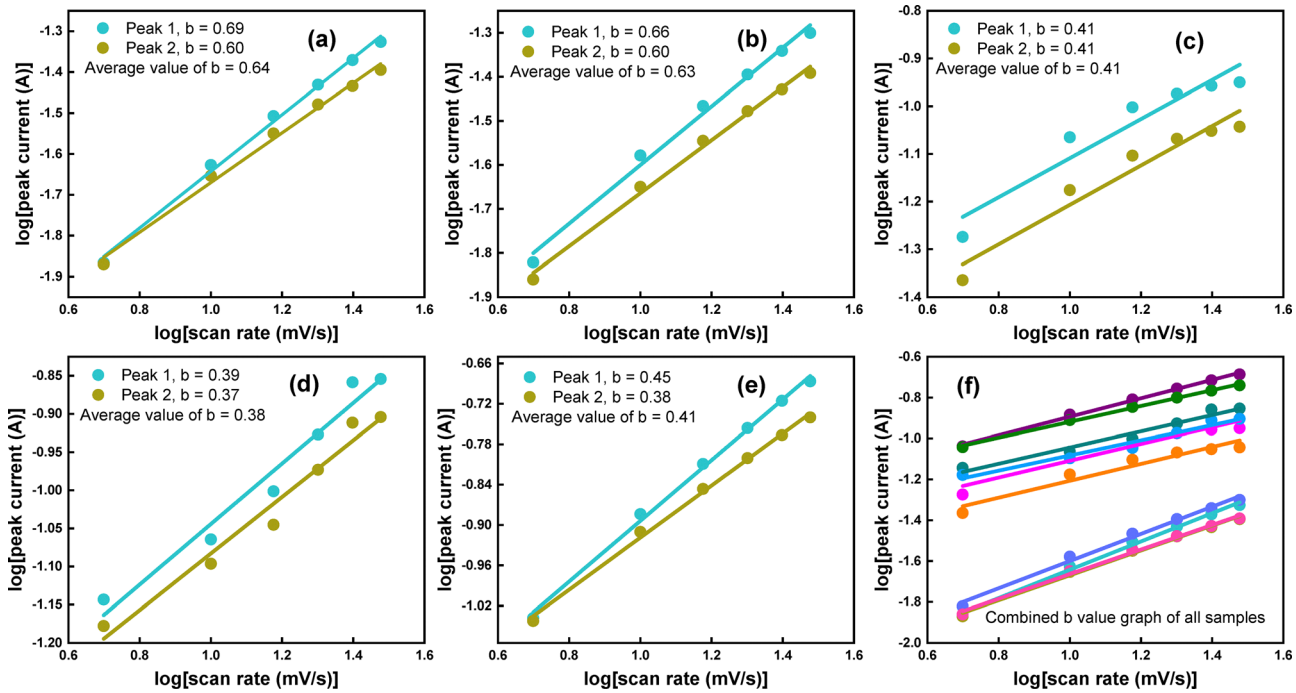

Fig. 5 (a)–(e) Values of b from the slope after linear fitting calculated from the CV curves at different scan rates, and (f) combined graph of anodic and cathodic peak current fitting of all samples.

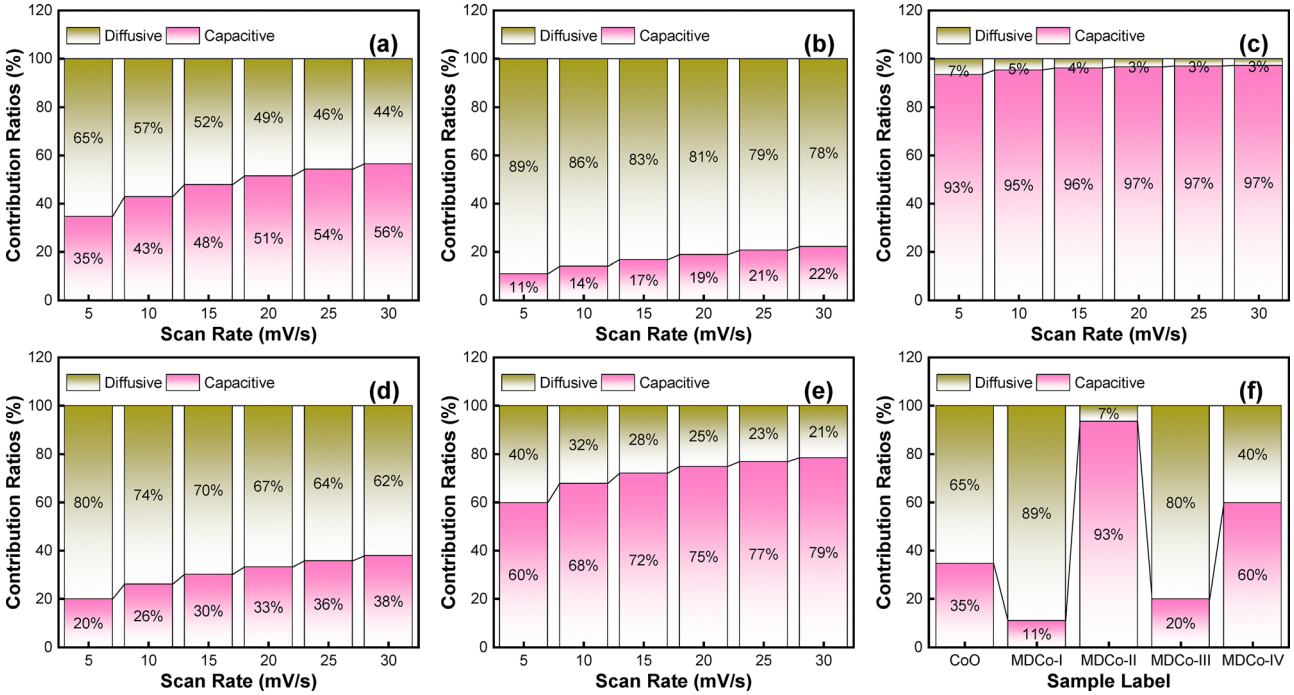

Fig. 6 (a)–(e) Ratios of capacitive and diffusive controlled processes for CoO, MDCoO-I, MDCoO-II, MDCoO-III, and MDCoO-IV, respectively, and (f) contribution ratios of individual samples at 5 mV s^{-1}.

confirmed by the CV results, and serves as clear evidence of the hybrid nature of the electrode material. The integration of Mn in MDCoO-I, MDCoO-II, MDCoO-III, and MDCoO-IV and rGO in MDCoO-III and MDCoO-IV, except pristine (Co_3O_4), has a significant influence on the discharge time. For example, doping of Mn at 0.04 molar ratio into Co_3O_4 demonstrated slightly better discharging durations (53.19 s) compared to the pristine CoO. This trend was observed to be more improved with an excellent discharging period of 310.66 s when a 0.08 molar ratio of Mn dopant was used. Further, improvements in the discharging duration of up to 507.16 s were achieved in the case of inclusion of 4% rGO in Co_3O_4 with Mn-doping of 0.04 molar ratio (MDCoO-III). Last but not least, the addition of 8% rGO into Co_3O_4 with Mn-doping of 0.08 molar ratio (MDCoO-IV) facilitated the highest discharging rate (877.42 s), which is attributed to the synergistically optimized integration of Mn and rGO into pristine Co_3O_4 (CoO). This analysis is based on the observations of GCD profiles shown in Fig. 7(a–e). These behaviors suggest that the incorporation of Mn and rGO enhanced both the energy storage capacity and the discharge durations. Furthermore, the addition of Mn and rGO contributed to substantial improvements in Q_s, ED, and PD. Due to the resemblance with hybrid charge storage mechanism-based type of SC, the observed GCD profiles were used to calculate the Q_s instead of the C_{sp} of the as-fabricated electrode series, supported by the expression stated in eqn (4):[14]

$$Q_s = I \times \Delta t/m \quad (4)$$

where I is the charging current, Δt is the discharge time, m is the loading mass, and V is the potential window. The Q_s values for all samples, calculated at different I_m, are illustrated in Table 3 and depicted graphically in Fig. 7(f). A gradual decrease in Q_s was observed with increasing current density, which can be attributed to the restricted accessibility of the active material for redox reactions under high current conditions.[40]

In addition to this, asymmetric assemblies of CoO, MDCoO-I, MDCoO-II, MDCoO-III, and MDCoO-IV were developed and their GCD profiles at various current densities are presented in Fig. 8(a–e). Activated carbon was considered as the negative electrode, and materials under investigation were employed as the cathode material deposited over the nickel foam substrate. Testing using a 2-electrode configuration in a 1 M KOH electrolyte was carried out, applying a galvanostatic current of 5, 10, 15, 20, and 25 mA. The charge storage mechanism, especially in the case of Mn-doped Co_3O_4@rGO, can be discussed as follows: during oxidation, OH^- ions are consumed in the pores of Mn-doped Co_3O_4@rGO, releasing electrons from Mn and Co and forming metal oxyhydroxide. During the reduction process, these ions return to the electrolyte as Mn and Co gain electrons. Meanwhile, K^+ ions are electrostatically adsorbed during oxidation and desorbed during reduction, returning to the bulk electrolyte. The prime objectives were to compute the ED and PD values of these materials precisely, which were subsequently evaluated using eqn (5) and (6):[14]

$$ED = C_{sp} \times V^2/3.6 \quad (5)$$

$$PD = ED \times 3600/\Delta t \quad (6)$$

The C_{sp}, Q_s, ED, and PD values obtained at different I_m are summarized in Table 4. The distinct plateaus observed in the

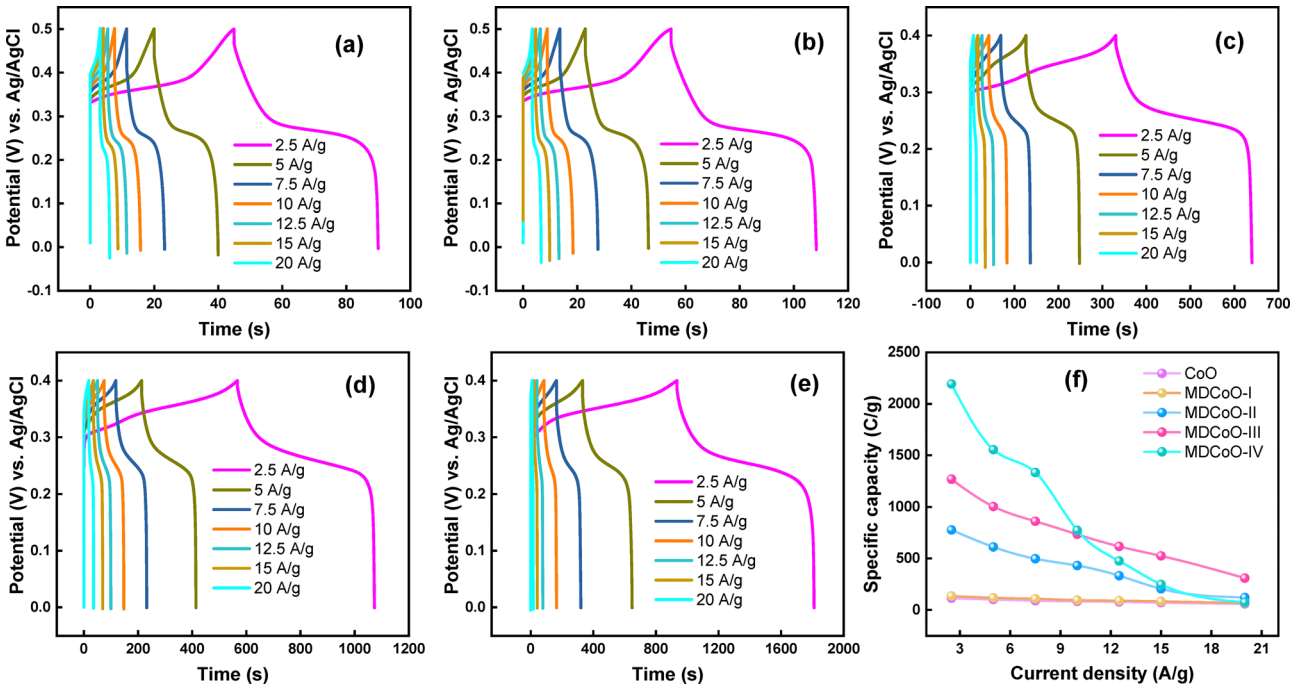

Fig. 7 GCD profiles at different current densities for (a) CoO, (b) MDCoO-I, (c) MDCoO-II, (d) MDCoO-III, (e) MDCoO-IV, and (f) current density *vs.* specific capacity.

Table 3 Specific capacity of CoO, MDCoO-I, MDCoO-II, MDCoO-III, and MDCoO-IV at multiple current densities

Sample	Current density (A g^{-1})	Discharge time (s)	Specific capacity (C g^{-1})
CoO	2.5	45.13	112.82
	5	19.95	99.79
	7.5	11.74	88.05
	10	8.21	82.17
	12.5	6.16	77.02
	15	4.61	69.18
	20	2.88	57.64
MDCoO-I	2.5	53.91	134.78
	5	23.27	116.36
	7.5	14.31	107.34
	10	9.37	93.78
	12.5	7.12	89.05
	15	5.44	81.60
	20	3.35	67.16
MDCoO-II	2.5	310.66	776.65
	5	122.26	611.30
	7.5	66.16	496.20
	10	42.98	429.86
	12.5	26.52	331.55
	15	13.63	204.46
	20	5.98	119.60
MDCoO-III	2.5	507.16	1267.91
	5	200.81	1004.07
	7.5	114.85	861.43
	10	73.39	733.93
	12.5	49.27	615.98
	15	34.95	524.31
	20	15.37	307.56
MDCoO-IV	2.5	877.42	2193.56
	5	310.84	1554.24
	7.5	177.59	1331.99
	10	77.23	772.39
	12.5	37.97	474.66
	15	16.42	246.36
	20	3.66	73.20

GCD profiles provide clear evidence of pseudocapacitive behavior, which is pronounced in all samples. Moreover, the ED and PD values indicate that binary metal oxides outperform single metal oxides as electrode materials. This enhancement can be attributed to the improved electrical conductivity and rate capability achieved through the strategic doping of transition metal oxides, effectively mitigating their inherent limitations. For instance, the CoO based electrode material demonstrated a C_{sp} of 67.60 F g^{-1} with an ED of 4.69 Wh kg^{-1} at a PD of 1250 W kg^{-1}, which is relatively lower than the energy storage capabilities of MDCoO-IV that yielded the highest values of C_{sp} of about 833.25 F g^{-1} along with an ED of 57.86 Wh kg^{-1} at a PD of 1250 W kg^{-1} compared to MDCoO-I, MDCoO-II, and MDCoO-III. In other words, MDCoO-IV facilitated 12.33 times higher energy storage capabilities in comparison to pristine CoO, with the highest PD of 6250 W kg^{-1} at 12.50 A g^{-1}. In a nutshell, the Ragone plot is depicted in Fig. 8(f). Parameters such as the particle size, morphology, and distribution play a crucial role in determining the electrochemical performance of these materials. Given the absence of prior electrochemical studies on the samples under investigation, a comparative analysis of the calculated ED and PD values with previously reported values from the literature is presented in Table 5.[25,43–49]

EIS was performed in the frequency range of 100 k–0.001 Hz to describe the transport of charge carriers. Fig. 9(a) indicates the combined Nyquist plots of CoO, MDCoO-I, MDCoO-II, MDCoO-III, and MDCoO-IV, and Fig. 9(b-f) shows the EIS curves simulated with the help of the corresponding circuit elements. In principle, the Nyquist plots show the relationship between the imaginary and real parts of the impedance, which are fundamental components. They offer essential insights into the kinetics as well as the

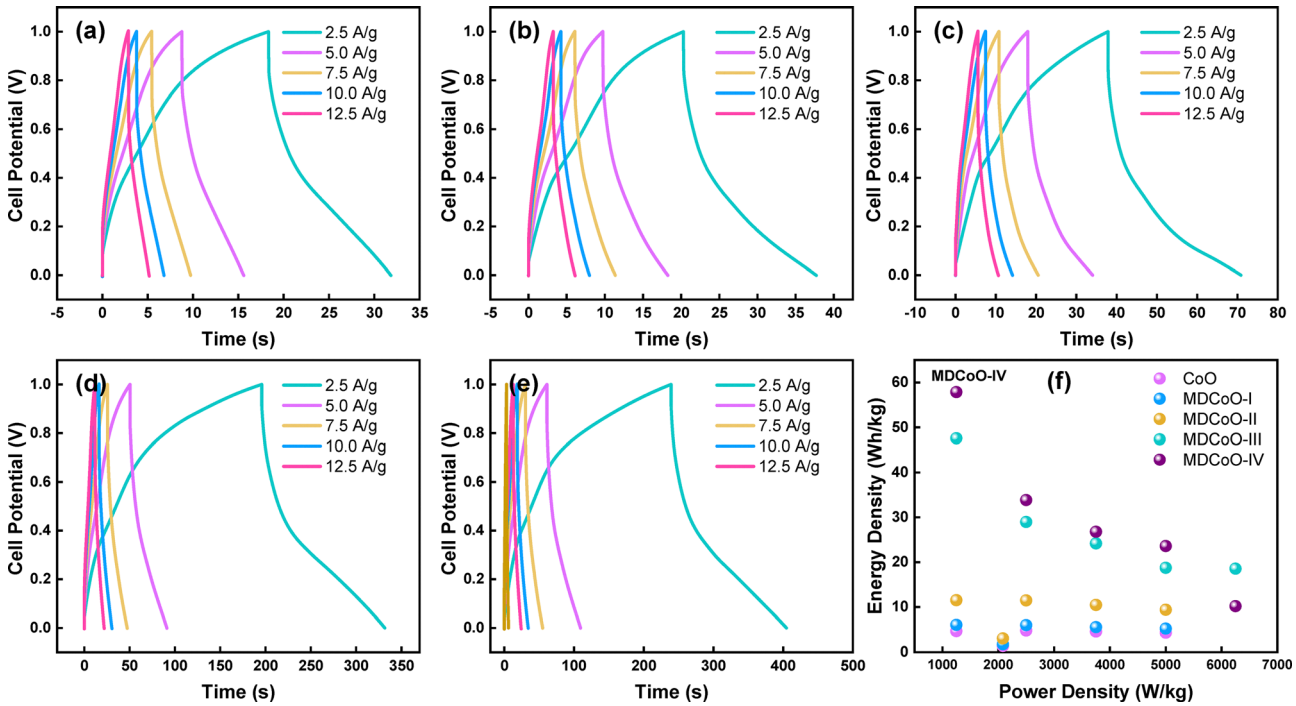

Fig. 8 GCD profiles at different current densities for (a) CoO, (b) MDCoO-I, (c) MDCoO-II, (d) MDCoO-III, and (e) MDCoO-IV, and (f) Ragone plot of all samples.

Table 4 Specific capacitance, specific capacity, energy density, and power density of CoO, MDCoO-I, MDCoO-II, MDCoO-III, and MDCoO-IV based asymmetric supercapacitors at multiple current densities

Sample	Current density ($A\ g^{-1}$)	Specific capacitance ($F\ g^{-1}$)	Specific capacity ($C\ g^{-1}$)	Energy density ($Wh\ kg^{-1}$)	Power density ($W\ kg^{-1}$)
CoO	2.5	67.60	33.80	4.69	1250
	5	69.50	34.75	4.82	2500
	7.5	66.15	33.075	4.59	3750
	10	62.40	31.20	4.33	5000
	12.5	67.60	9.91	1.37	2083
MDCoO-I	2.5	87.55	43.77	6.07	1250
	5	86.50	43.25	6.00	2500
	7.5	80.40	40.20	5.58	3750
	10	75.60	37.80	5.25	5000
	12.5	87.55	12.62	1.75	2083
MDCoO-II	2.5	165.90	82.95	11.52	1250
	5	165.20	82.60	11.47	2500
	7.5	150.75	75.37	10.46	3750
	10	135.20	67.60	9.38	5000
	12.5	165.90	22.12	3.07	2083
MDCoO-III	2.5	685.05	342.52	47.57	1250
	5	417.02	208.50	28.95	2500
	7.5	348.30	174.15	24.18	3750
	10	270.03	135.01	18.75	5000
	12.5	267.01	133.50	18.54	6250
MDCoO-IV	2.5	833.25	416.62	57.86	1250
	5	487.50	243.75	33.85	2500
	7.5	385.65	192.82	26.78	3750
	10	339.60	169.80	23.58	5000
	12.5	147.01	73.50	10.20	6250

ion transportation between the electrode materials and the electrolyte interface. The plots consisted of an approximately inclined straight line and a semicircle arc in the low- and high-frequency regions. In the high-frequency region, the point that crosses the real axis represents the resistance owing to the electrolyte or solution known as R_s. In the intermediate frequency region, the diameter of the semicircle arc appears, denoting the charge transfer resistance (R_{ct}), while the slope of the inclined line indicates the Warburg impedance.

Comprehending the analysis, Fig. 9(a) shows the Nyquist plot of CoO, indicating that when rGO was added at low concentrations (*i.e.*, 4%), the semicircle's diameter decreases slightly, causing a minor reduction in R_{ct}. This likely results from improved conductivity due to the uniform dispersion of rGO into the redox-active channels. In addition to this, to estimate the impedance parameters due to the complex reaction kinetics at the electrode/electrolyte interface, an equivalent circuit was designed. In this circuit, each element played a unique role. For instance, R_1 was used to measure solution resistance, while resistor R_2 was placed in parallel with the capacitive element (C_3), to calculate the double layer capacitance value, and connected in series and parallel with constant phase elements Q_3 and Q_5 to smoothly fit the experimental data points, which represent the non-ideal capacitive behaviors associated with the stability of the electrode–electrolyte interface. An additional Warburg element (W_1) in series at the end was included, corresponding to the ion diffusion from the bulk electrolyte to the pores of the electrode material, and the experimental data were simulated using EC Lab V11.60 Software, as shown in Fig. 9(b–f). Symbolic circles represent the experimental data, while the simulated data are indicated by a line to estimate the R_{ct} and Warburg impedance parameters, respectively. The values of the fitting parameters for all samples from the simulation results are tabulated in

Table 5 Comparison of performance parameters of different electrode materials

Sample	Specific capacitance (F g^{-1})	Energy density (Wh kg^{-1})	Power density (W kg^{-1})	Cyclic stability (%)	Ref.
Mn-doped Co_3O_4	105.8	33	748.10	92.8% after 5k cycles	25
Cr-doped Co_3O_4	669.28	42.5	1295.73	100% after 5k cycles	43
Mn-doped Co_3O_4	1674	13.80	195k	91.48% after 5k cycles	44
Co_3O_4/rGO	273.3	16.47	599	91% after 5k cycles	45
NiO/Co_3O_4/rGO	1422	76.2	795.3	100% after 10k cycles	46
NiO/Co_3O_4	980	23.7	1396.7	89% after 5k cycles	47
Mn-doped Co_3O_4	668.4	25.88	359.5	104% after 10k cycles	48
Mo_3O_4/rGO	427	34.3	0.47k	106% after 10k cycles	49
Mn-doped Co_3O_4/rGO//AC	833.25	57.86	1250	87.27% after 10k cycles	This work

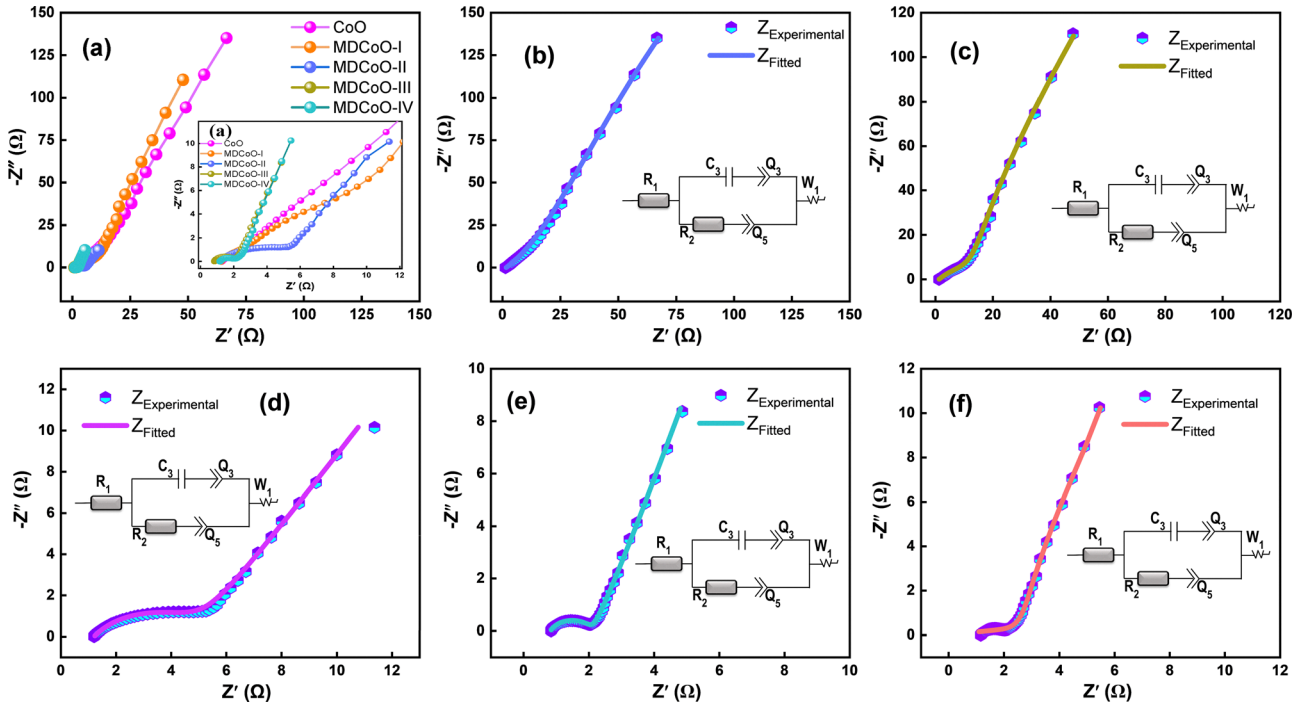

Fig. 9 (a) Combined EIS spectra for all the fabricated electrodes and (b)–(f) EIS fitting spectra of CoO, MDCoO-I, MDCoO-II, MDCoO-II, MDCoO-III, and MDCoO-IV using Biologic EC Lab V11.60 software.

Table 6. It can be deduced that, in EIS curve fitting of each sample, each individual element played a distinct and significant role, depending on the EIS spectra, indicating that ion kinetics heavily depend on the composition of the electrode material.

In more detail, Fig. 9(f) shows that for MDCoO-IV, increasing rGO to 8% causes the semicircle's diameter to shrink further, but less than for MDCoO-III, and tilt towards the *y*-axis, indicating the most favorable R_{ct} and ion diffusion compared to that of CoO. This notable reduction in R_{ct} is due to the higher rGO content, which enhances electrical conductivity and charge transportation compared to the pure CoO. The Nyquist plots, showing linear segments at low frequencies, suggest Warburg impedance associated with ion diffusion in the electrolyte. The sharp decrease in the slope of the linear region in MDCoO-IV compared to that of all other electrode materials indicates highly efficient ion transport, demonstrating that rGO improves the electrochemical performance of the material.

Table 6 Values of elements for the corresponding fit circuit. R_1 = R_s, R_2 = R_{ct}, C_1 = capacitance, Q_3, Q_5 = constant phase elements, and W_1 = Warburg impedance

Sample	R_1 (Ω)	R_2 (Ω)	C_1 (mF)	Q_3 (F $s^{(a-1)}$)	Q_5 (F $s^{(a-1)}$)	W_1 (Ω)
CoO	1.29	4.25	0.21	0.50	0.04	12.97
MDCoO-I	1.23	3.28	3.80	1.78	0.07	8.23
MDCoO-II	1.19	4.09	0.05	1.59	0.02	2.13
MDCoO-III	0.83	0.89	0.89	0.02	0.09	1.96
MDCoO-IV	1.15	1.20	5.30	0.01	0.45	1.38

3.5. Ion transport properties

3.5.1. Diffusion coefficient. The study of diffusion dynamics plays a crucial role in describing the ion transport properties of energy storage devices, which fundamentally rely on evaluating the diffusion coefficient. This coefficient defines the mobility of ions from areas of higher concentration to regions of lower concentration. Consequently, the performance of these energy storage technologies depends entirely on diffusion dynamics. From this

perspective, the study employs an experimental approach using GITT. The conditions set during the experiment are as follows: the relaxation time was established at 10 min, and currents of 1, 5, and 10 mA were applied, with 3 and 6 M KOH electrolyte concentrations. The experiments conducted under these conditions yielded discharge/charge profiles with varying potentials, as shown in Fig. 10(a–c) for CoO, MDCoO-I, and MDCoO-III in a 3 M KOH electrolyte. Additionally, various experiments using this technique were conducted with MDCoO-IV in 3 and 6 M KOH electrolyte concentrations at 1, 5, and 10 mA to observe variations in diffusion dynamics, as depicted in Fig. 10(d–i), and to propose the best outcomes after careful comparison.

The calculations of diffusion coefficient were carried out using eqn (7), as stated below:[19,50–53]

$$D_{K^+} = \frac{4}{\pi\tau}\left(\frac{m_b V_m}{M_B S}\right)^2 \left(\frac{\Delta E_s}{\Delta E_t}\right)^2 \quad (7)$$

In this equation, D_{K+} reflects the diffusion coefficient for K^+ ions associated with the KOH electrolyte; on the other hand, different parameters like τ, products $m_b V_m$ and $M_B S$, and $\Delta E_s/\Delta E_t$ stand for relaxation time, loading mass and molar volume, and molar mass of the active material and surface area it covers on the electrode, and ratio of potential changes in steady state to the potential changes during charging/discharging phases. Finally, the values of the diffusion coefficient computed from the above equation are listed in Tables 7 and 8. It is evident that variations in electrolyte concentration and current density have a significant effect on the diffusion dynamics of MDCoO-IV. For instance, at 1, 5, and 10 mA in the 3 M KOH electrolyte, the values of the diffusion coefficient estimated for MDCoO-IV are 2.15×10^{-13}, 3.41×10^{-13}, and 5.51×10^{-13} $m^2 s^{-1}$, which are pretty higher than the diffusion dynamics in 6 M KOH and CoO, MDCoO-I, MDCoO-II, and MDCoO-III. Thus, it can be deduced that MDCoO-IV demonstrated excellent diffusion dynamics at a lower concentration of KOH than at higher current densities. At 10 mA, it exhibited remarkable ion transport properties in 3 M KOH due to its high potential to accelerate ions under these conditions. Under these optimized conditions, MDCoO-IV

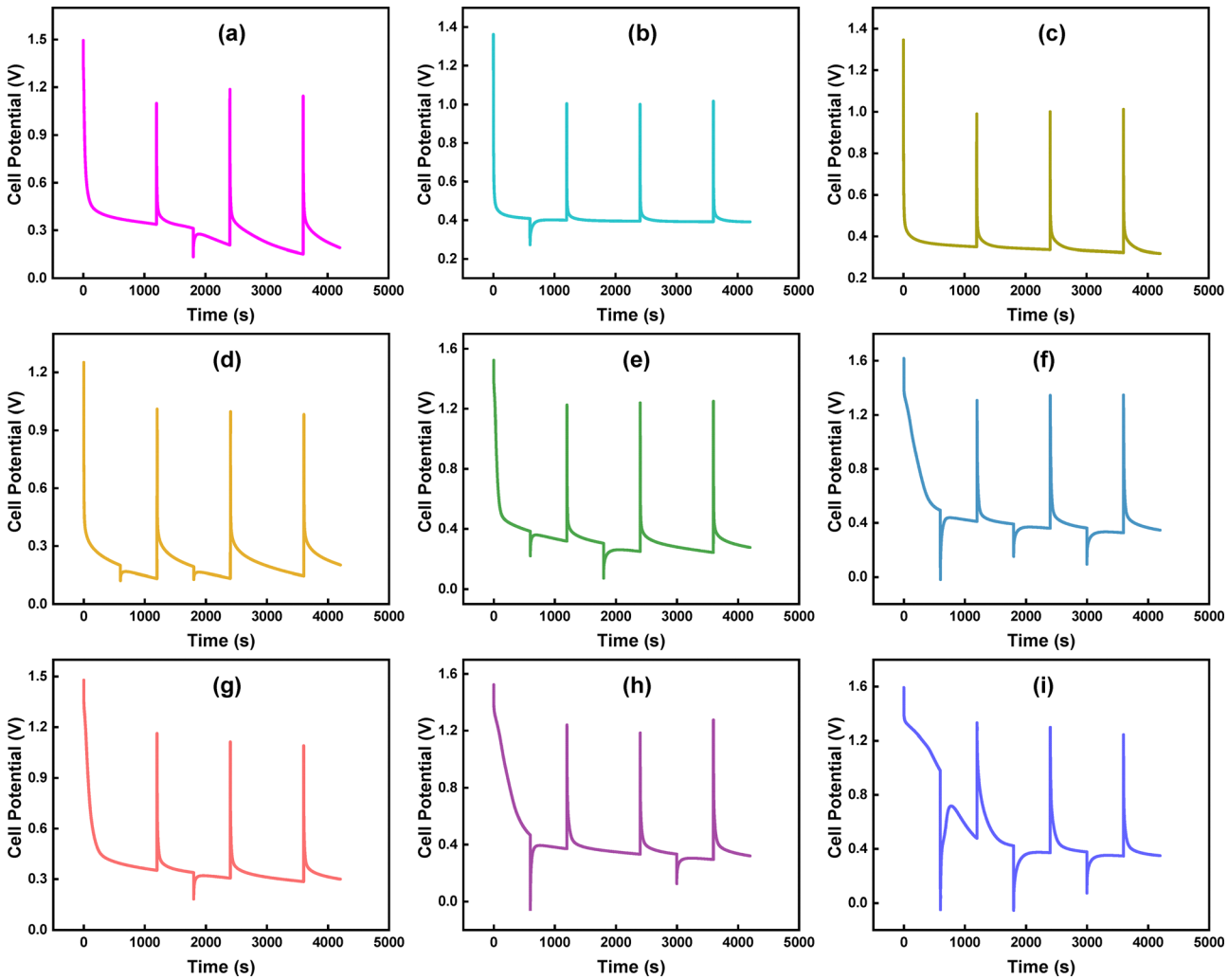

Fig. 10 (a)–(c) Discharging/charging profiles of CoO, MDCoO-I, and MDCoO-III based electrode materials in 3 M KOH and (d)–(i) discharging/charging profiles of the MDCoO-IV//AC based designed device obtained using the GITT to investigate the diffusion dynamics at different currents of 1, 5, and 10 mA in 3 and 6 M KOH electrolyte concentrations.

Table 7 Diffusion coefficients for CoO, MDCoO-I, MDCoO-III, and MDCoO-IV in 3 M KOH

Sample	Ionic conductivity (S cm^{-1})	Transference number	Rate constant (cm s^{-1})	Exchange current density (A g^{-1})	Diffusion coefficient (m^2 s^{-1})
CoO	0.055	0.090	6.26×10^{-8}	0.0060	1.02×10^{-13}
MDCoO-I	0.058	0.130	8.11×10^{-8}	0.0078	1.41×10^{-13}
MDCoO-II	0.060	0.358	6.50×10^{-8}	0.0062	—
MDCoO-III	0.085	0.297	2.99×10^{-7}	0.0288	1.67×10^{-13}
MDCoO-IV	0.062	0.454	2.21×10^{-7}	0.0214	2.15×10^{-13}

Table 8 Diffusion coefficients of MDCoO-IV at different current densities and electrolyte concentrations

Sample	Current (mA)	Electrolyte concentration	Diffusion coefficient (m^2 s^{-1})	Electrolyte concentration	Diffusion coefficient (m^2 s^{-1})
MDCoO-IV	1	3 M	2.15×10^{-13}	6 M	9.51×10^{-15}
MDCoO-IV	5	3 M	3.41×10^{-13}	6 M	3.29×10^{-14}
MDCoO-IV	10	3 M	5.51×10^{-13}	6 M	1.08×10^{-14}

appeared to be the best among the fabricated electrode series for enhanced energy storage performance-based devices.

3.5.2. Ionic conductivity. The electrochemical performance of electrode materials primarily depends on their ion conduction capability, which is influenced by the ionic radii and surface chemistry of the material. Additionally, the rate of redox activity heavily relies on the surface characteristics of the electrode material, which directly affect the performance of energy storage devices. Therefore, estimating such attributes is crucial in defining the overall performance of the energy storage device, as measured by the following general relationship (eqn (8)) from EIS parameters:

$$\sigma = \frac{l}{R_i \times A} \tag{8}$$

In this relationship, σ reflects the ionic conductivity in S cm^{-1}, l is associated with the thickness of the electrode, which was measured to be 0.9 mm by using a digital vernier caliper, R_i is the solution resistance (ionic resistance) that usually appears before the semicircle in EIS spectra, and A represents the electrode's effective surface area, which has been estimated from a vernier caliper.[50,51,54] In this study, the estimated ionic conductivities are listed in Table 7. The variation in the values of ionic conductivities of all electrode materials is due to polarization effects and temperature variations during electrochemical testing, which directly influence the mobility of ions within the solution and in the layers of the electrode material. Based on these characteristics, the fabricated electrode series demonstrated excellent potential in advanced energy storage technologies.

3.5.3. Transference number. In addition to the ion transport property, which shows notable variation from sample to sample, assessing the proportion of each ion type (anions and cations), commonly referred to as the transference number in this context, is more important. This number defines the contribution of each ion type to the overall conduction phenomenon, which in turn impacts the device's overall performance. Based on the information for cations, one can deduce the value for anions, as it is the sum of each type, which has a maximum value of 1. For instance, the transference number for cations can be determined from the following relationship (eqn (9)), proposed by Sorenson and Jacobsen:

$$t_+ = \frac{1}{1 + Z_d(0)/R_b} \tag{9}$$

In this equation, two parameters (Z_d and R_b) are variable parameters estimated from EIS and are dependent on the electrochemical conditions.[55] These parameters represent the Warburg diffusion (Z_d) and bulk resistance (R_b), which correspond to the solution or series resistance expressed in Ohms. The values of the cation transference number, calculated from the previously mentioned equation for all samples, are reported in Table 7. The primary objective of this analysis was to investigate the contribution of each type of ion and to analyze how variations in the composition of the electrode material reveal deviations in ionic conduction under optimized conditions. Therefore, studying the features of ion transport in depth is essential because specific mathematical relationships are particularly fascinating from the perspective of SC applications.

3.5.4. Rate constant. Another crucial analysis is the rate constant, which defines the number of charge carriers transferred at the electrode/electrolyte interface during redox reactions. It varies from material to material and electrolyte to electrolyte because, in this study, the charge transfer resistance is the variable parameter defined by the resistance presented by charge carriers at the electrode/electrolyte interface. Such ion transport properties significantly influence the overall performance of the energy storage device and have the potential to impact electrochemistry for scientists and researchers. To compute the variation of the rate constant from sample to sample, it has been quantified in eqn (10):[52,56]

$$K = \frac{RT}{F^2 \times R_{ct} \times C} \tag{10}$$

Herein, K represents the rate constant (cm s^{-1}) and RT represents the product of temperature and the universal gas constant. F and C represent Faraday's constant and total molar concentration of electrolytic species, and R_{ct} represents charge transfer resistance

in Ohms. The rate of the reaction was estimated for each sample in the current study and is provided in Table 7. From here, the difference in reaction rate between CoO and MDCoO-IV becomes apparent, which is attributed to the reaction kinetics of the electrode material under optimized conditions and is influenced by polarization effects and other factors.

3.5.5. Exchange current density. Additionally, concerning ion transport properties, the key parameter is the exchange current density, which defines the effectiveness of charge carriers and improves their kinetics. It quantifies the balanced charge transfer at equilibrium, where the rates of oxidation and reduction are typically equal. The higher the exchange current density, the better the performance of the energy storage system. The property of an electrochemical system can be estimated using eqn (11):[56]

$$J_0 = \frac{RT}{n \times F \times R_{ct}} \quad (11)$$

Here, two additional parameters are the primary focus of this equation. The variable J_0 represents the exchange current density (A g^{-1}), while n corresponds to the number of electrons transferred during the redox activity. The values of exchange current density for each sample are listed in Table 7. The table illustrates the fluctuation of exchange current density from sample to sample in this study.

3.6. Asymmetric supercapacitor device

After a thorough evaluation and careful consideration of the energy storage capabilities of all fabricated electrodes, an asymmetric device using MDCoO-IV has been developed with a focus on practical applications for future energy storage technologies. This device is designed so that the working electrode (MDCoO-IV) serves as a cathode, while activated carbon acts as an anode, and it is tested in a 6 M KOH electrolyte solution. The performance and stability of the MDCoO-IV//AC-based device have been assessed through extensive electrochemical investigations employing various techniques, such as CV at different potential windows and scan rates, GCD at different potential ranges and I_m, and EIS with an applied AC signal of 10 mA amplitude.

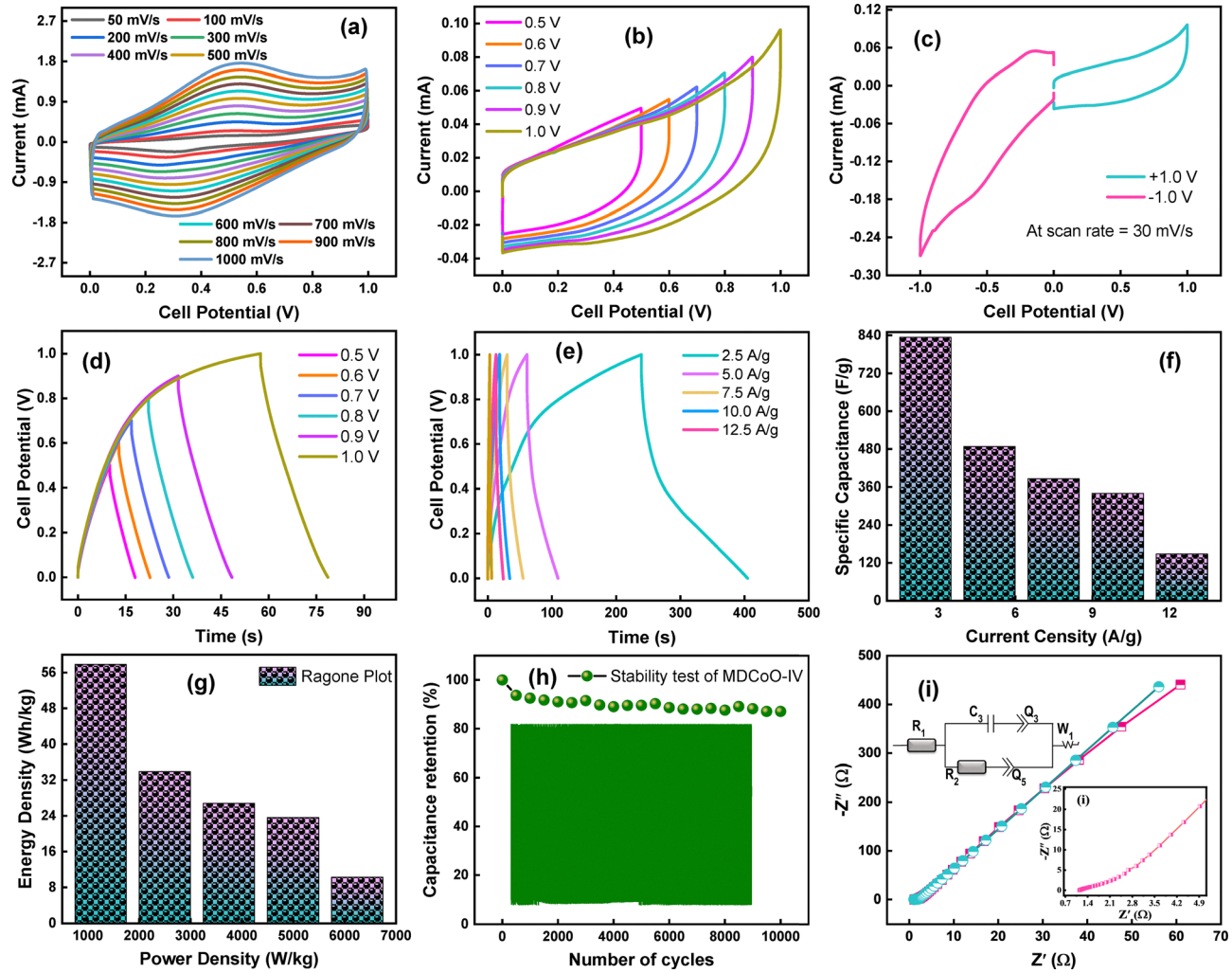

Fig. 11 (a) CV curves of MDCoO-IV//AC at multiple scan rates, (b) CV curves at variable potential windows, (c) CV curves at positive and negative potential windows, (d) and (e) GCD profiles of MDCoO-IV//AC at different current densities and potential windows, (f) current density *vs.* specific capacitance, (g) Ragone plot, (h) stability test, and (i) EIS analysis of MDCoO-IV//AC.

To further understand the electrochemical performance of MDCoO-IV//AC, the reversibility of the system has been studied over a potential range of 0 to 1.0 V at various scan rates, ranging from 50 to 1000 mV s^{-1} in 100 mV s^{-1} increments after 10 cycles of CV at 50 mV s^{-1} to stabilize the electrode/electrolyte contact, as shown in Fig. 11(a). The maintained symmetry of the redox peaks, with almost equal increases as the scan rate increases, suggests excellent stability of the electrode/electrolyte interface. The lack of abrupt jumps in the redox peaks toward higher currents further confirms the maintained stability at higher potential windows, as shown in Fig. 11(b). In addition, the reversibility of the designed device has also been examined over the range of 0 to −1.0 V and 0 to +1.0 V, as shown in Fig. 11(c).

More importantly, this study evaluated energy storage capabilities, which are generally estimated from the energy storage device's ED and PD. These values have been determined through GCD testing at various I_m and potential windows. The variable potential window of MDCoO-IV//AC enabled us to select the optimized limit for achieving better results, as shown in Fig. 11(d). For instance, from 0 to 1.0 V, the charging and discharging limits fall within this range, indicating the enhanced energy storage ability of MDCoO-IV//AC, as illustrated in Fig. 11(e). At different I_m, the designed device demonstrated remarkable rate performance, even at higher current densities, due to the system's stability. Thus, the energy and power densities of such a system, owing to the pseudocapacitive charge storage mechanism, yielded improved performance of approximately 57.86 Wh kg^{-1} with 1250 W kg^{-1} at 2.5 A g^{-1}. The trend against I_m and capacitance is showcased in Fig. 11(f and g). Moreover, the highest PD (6250 W kg^{-1}) of MDCoO-IV//AC has been achieved at 10.20 Wh kg^{-1}. The stability of this energy storage device has been determined to be 87.27% following extensive GCD testing of approximately 10 000 cycles, which is evident from Fig. 11(h).

EIS analysis of the MDCoO-IV//AC-based device design revealed a significant improvement in ion transport properties, along with faster reaction kinetics. The rise in the *y*-component indicated increased reactive elements compared to the resistive elements on the *x*-axis. Precise estimations of R_s, R_{ct}, and W were obtained from the impedance spectra in Fig. 11(i) by simulating experimental data using EC Lab Software. The Randle circuit used is shown in Fig. 11(i) as an inset, illustrating possible circuit elements such as resistors, capacitors, constant phase elements, and modified Warburg impedance. The values of R_s, R_{ct}, and Warburg impedance are 1.26, 0.96, and 1.55 Ω, respectively.

4. Conclusion

In conclusion, the fabricated electrode series of Co_3O_4 with varying doping levels of Mn (0.08 and 0.04 molar ratios) and added rGO content (4% and 8%), using hydrothermal and solvothermal synthesis techniques, underwent various characterization methods such as XRD, FESEM, EDX, CV, GCD, and EIS. A comprehensive electrochemical investigation of this series through a 3-electrode configuration indicated that $Co_{2.92}Mn_{0.08}O_4$@8%rGO demonstrated an exceptional rate capability compared to all others. At this point, the specific capacity of this composite was observed to be 2820 C g^{-1} at 5 mV s^{-1}, as determined from CV analysis. Furthermore, the improved ion transport properties, such as enhanced ion conductivity (0.62 S cm^{-1}), transference number (0.45), rate constant (2.21 × 10^{-7} cm s^{-1}), exchange current density (0.021 A g^{-1}), and good diffusion dynamics (5.51 × 10^{-13} m^2 s^{-1}), were noteworthy in proposing the best device. In addition, an asymmetric device with full testing achieved the highest energy and power density of approximately 57.86 Wh kg^{-1} at 1250 W kg^{-1}, with a long lifespan of 87.27% after 10 000 continuous GCD cycles. These notable outcomes highlighted the potential of such electrode materials with improved device performance in practical applications.

Conflicts of interest

The authors declare that there are no financial or any other types of conflicts of interest to declare for this submission.

Data availability

Data will be made available on request.

Acknowledgements

The authors would like to acknowledge the Ongoing Research Funding Program (ORF-2026-43), King Saud University, Riyadh, Saudi Arabia.

References

1 S. Liu, L. Kang and S. C. Jun, Challenges and strategies toward cathode materials for rechargeable potassium-ion batteries, *Adv. Mater.*, 2021, **33**, 2004689.
2 J. Sun, C. Xu and H. Chen, A review on the synthesis of $CuCo_2O_4$-based electrode materials and their applications in supercapacitors, *J. Mater.*, 2021, **7**, 98–126.
3 A. Z. A. L. Shaqsi, K. Sopian and A. Al-Hinai, Review of energy storage services, applications, limitations, and benefits, *Energy Rep.*, 2020, **6**, 288–306.
4 D. R. Patil, B. Koteswararao, K. Begari, A. Yogi, M. Moussa and D. P. Dubal, Cobalt cyclotetraphosphate ($Co_2P_4O_{12}$): a new high-performance electrode material for supercapacitors, *ACS Appl. Energy Mater.*, 2019, **2**, 2972–2981.
5 G.-F. Zhang, P. Qin and J.-M. Song, Facile fabrication of Al_2O_3-doped Co_3O_4/graphene nanocomposites for high performance asymmetric supercapacitors, *Appl. Surf. Sci.*, 2019, **493**, 55–62.
6 M. Aadil, S. Zulfiqar, M. Shahid, S. Haider, I. Shakir and M. F. Warsi, Binder free mesoporous Ag-doped Co_3O_4 nanosheets with outstanding cyclic stability and rate capability for advanced supercapacitor applications, *J. Alloys Compd.*, 2020, **844**, 156062.

7 Y.-R. Zhu, P.-P. Peng, J.-Z. Wu, T.-F. Yi, Y. Xie and S. Luo, Co_3O_4@ $NiCo_2O_4$ microsphere as electrode materials for high-performance supercapacitors, *Solid State Ionics*, 2019, **336**, 110–119.
8 J. A. Goudar, T. SN, S. Chapi, M. MV, M. R. Saeb and M. Salami-Kalajahi, Cobalt-based materials in supercapacitors and batteries: A review, *Adv. Energy Sustain. Res.*, 2025, **6**, 2400271.
9 H. Yao, F. Zhang, G. Zhang, H. Luo, L. Liu, M. Shen and Y. Yang, A novel two-dimensional coordination polymer-polypyrrole hybrid material as a high-performance electrode for flexible supercapacitor, *Chem. Eng. J.*, 2018, **334**, 2547–2557.
10 L. Xu, D. Sun, S. Lv, G. Tian, G. Wang, B. Wang, L. Zhang and S. Wang, Novel semiconductor materials for advanced wide temperature range supercapacitors, *J. Mater. Chem. A*, 2025, **13**(10), 6954–6992.
11 K. Prajapat, U. Mahajan, A. Kumar, M. Dhonde, K. Sahu, S. Vyas, Y. M. Riyad and M. Zeinhom, *Sustainable Mater. Technol.*, 2025, **35**, 173–338.
12 P. Du, W. Wei, D. Liu, H. Kang and P. Liu, Fabrication of hierarchical carbon layer encapsulated polyaniline core-shell structure nanotubes and application in supercapacitors, *Chem. Eng. J.*, 2018, **335**, 373–383.
13 A. Mohammadpour-Haratbar, P. Kiaeerad, S. Mazinani, A. M. Bazargan and F. Sharif, Bimetallic nickel–cobalt oxide nanoparticle/electrospun carbon nanofiber composites: Preparation and application for supercapacitor electrode, *Ceram. Int.*, 2022, **48**, 10015–10023.
14 A. Iqbal, R. Nadeem, A. Shakoor, M. Luqman, M. Mehak, M. U. Salman, S. M. Ramay, F. Ahmad and S. Atiq, Enhanced ionic conductivity in synergistically developed $NiMnO_3$/CNTs nanocomposite electrode material in hybrid capacitors, *J. Energy Storage*, 2025, **134**, 118207.
15 S. Zawar, S. Atiq, S. Riaz and S. Naseem, Correlation between particle size and magnetic characteristics of Mn-substituted $ZnFe_2O_4$ ferrites, *Superlattices Microstruct.*, 2016, **93**, 50–56.
16 A. Kanwade, S. Gupta, A. Kankane, M. K. Tiwari, A. Srivastava, J. A. K. Satrughna, S. C. Yadav and P. M. Shirage, Transition metal oxides as a cathode for indispensable Na-ion batteries, *RSC Adv.*, 2022, **12**, 23284–23310.
17 J. Yu, Z. Hou, H. Zhang and X. Zhou, Synergistic coupling of MnS/Ni_3S_2 and $Co(OH)_2$ nanosheets as binder-free electrode materials for asymmetric supercapacitors with enhanced performance, *Fuel*, 2024, **357**, 129754.
18 A. Gowdhaman, S. A. Kumar, D. Elumalai, C. Balaji, M. Sabarinathan, R. Ramesh and M. Navaneethan, Ni-MOF-derived NiO/Ni/r-GO nanocomposite as a novel electrode material for high-performance asymmetric supercapacitor, *J. Energy Storage*, 2023, **61**, 106769.
19 A. Hussain, A. Tufail, A. Shakoor, M. Mehak, M. S. Akhtar, S. M. Ramay, S. Sarwar and S. Atiq, Synergistically tailored ionic conduction and transport in ZnO/CNTs based electrodes with enhanced electrochemical efficiency in supercapacitors, *Electrochim. Acta*, 2025, 146736.
20 A. F. Alem, A. K. Worku, D. W. Ayele, T. A. Wubieneh, A. A. Teshager, B. T. Admasu, M. A. Teshager, A. A. Asege, M. D. Ambaw and M. A. Zeleke, Ag-doped Co_3O_4 nanoparticles for high-performance supercapacitor application, *Heliyon*, 2023, **9**, e13286.
21 H. Chen, J. Wang, F. Liao, X. Han, Y. Zhang, C. Xu and L. Gao, Uniform and porous Mn-doped Co_3O_4 microspheres: Solvothermal synthesis and their superior supercapacitor performances, *Ceram. Int.*, 2019, **45**, 11876–11882.
22 S. Deng, X. Xiao, G. Chen, L. Wang and Y. Wang, Cd doped porous Co_3O_4 nanosheets as electrode material for high-performance supercapacitor application, *Electrochim. Acta*, 2016, **196**, 316–327.
23 A. Karthikeyan and R. Mariappan, Characterization and electrochemical performance of Mn-doped Co_3O_4 nanoparticles for supercapacitor applications, *J. Mater. Sci.: Mater. Electron.*, 2023, **34**, 2092.
24 A. Karthikeyan, R. Mariappan, E. Krishnamoorthy and R. Bakkiyaraj, Effect of Nickel doping on Cobalt Oxide nanoparticles for energy storage applications, *Ionics*, 2024, **30**, 2069–2082.
25 J. Wang, H. Zhang, H. Duan, H. Zhao, J. Qi, B. Ma and H. Fan, Boosting the electrochemical storage properties of Co_3O_4 nanowires by the Mn doping strategy with appropriate Mn doping concentrations, *ACS Omega*, 2024, **9**, 6955–6964.
26 H. J. Trinity Rabecca, Y. Priyajanani, S. Manivannan and A. J. C. Lourduraj, Investigation of electrochemical behavior of Co_3O_4–Mn_2O_3/rGO nanocomposite for supercapacitor applications, *J. Mater. Sci.: Mater. Electron.*, 2023, **34**, 1390.
27 G. A. Jeffery, Elements of X-ray diffraction (Cullity, BD), (1957).
28 G. Ercolino, A. Grodzka, G. Grzybek, P. Stelmachowski, S. Specchia and A. Kotarba, The Effect of the Preparation Method of Pd-Doped Cobalt Spinel on the Catalytic Activity in Methane Oxidation Under Lean Fuel Conditions, *Top. Catal.*, 2017, **60**, 333–341.
29 Z. Shi, G. Sun, R. Yuan, W. Chen, Z. Wang, L. Zhang, K. Zhan, M. Zhu, J. Yang and B. Zhao, Scalable fabrication of $NiCo_2O_4$/reduced graphene oxide composites by ultrasonic spray as binder-free electrodes for supercapacitors with ultralong lifetime, *J. Mater. Sci. Technol.*, 2022, **99**, 260–269.
30 S. Liu, H. Nan, L. Li, T. Qin, L. Cai, W. Zhang and W. Zheng, Unlocking the optimum supercapacitance of Co_3O_4 by reducing the Co valence state via Mn doping, *Mater. Today Commun.*, 2021, **28**, 102665.
31 B. Babakhani and D. G. Ivey, Improved capacitive behavior of electrochemically synthesized Mn oxide/PEDOT electrodes utilized as electrochemical capacitors, *Electrochim. Acta*, 2010, **55**, 4014–4024.
32 J. Gomez and E. E. Kalu, High-performance binder-free Co–Mn composite oxide supercapacitor electrode, *J. Power Sources*, 2013, **230**, 218–224.
33 B. Babakhani and D. G. Ivey, Investigation of electrochemical behavior of Mn–Co doped oxide electrodes for electrochemical capacitors, *Electrochim. Acta*, 2011, **56**, 4753–4762.
34 J.-K. Chang, M.-T. Lee, C.-H. Huang and W.-T. Tsai, Physicochemical properties and electrochemical behavior of binary manganese–cobalt oxide electrodes for supercapacitor applications, *Mater. Chem. Phys.*, 2008, **108**, 124–131.

35 H. Chen, J. Wang, F. Liao, X. Han, Y. Zhang, C. Xu and L. Gao, Uniform and porous Mn-doped Co_3O_4 microspheres: Solvothermal synthesis and their superior supercapacitor performances, *Ceram. Int.*, 2019, **45**, 11876–11882.

36 S. Zawar, G. Ali, G. M. Mustafa, S. A. Patil, S. M. Ramay and S. Atiq, Mn0.06Co2.94O4 nano-architectures anchored on reduced graphene oxide as highly efficient hybrid electrodes for supercapacitors, *J. Energy Storage*, 2022, **50**, 104298.

37 T. Uzzaman, S. Zawar, M. T. Ansar, S. M. Ramay, A. Mahmood and S. Atiq, Electrochemical performance of $NiFe_2O_4$ nanostructures incorporating activated carbon as an efficient electrode material, *Ceram. Int.*, 2021, **47**, 10733–10741.

38 H. Chen, J. Wang, F. Liao, X. Han, C. Xu and Y. Zhang, Facile synthesis of porous Mn-doped Co_3O_4 oblique prisms as an electrode material with remarkable pseudocapacitance, *Ceram. Int.*, 2019, **45**, 8008–8016.

39 Q. Tian, X. Wang, G. Huang and X. Guo, Nanostructured $(Co, Mn)_3O_4$ for high capacitive supercapacitor applications, *Nanoscale Res. Lett.*, 2017, **12**, 214.

40 T. Yao, X. Guo, S. Qin, F. Xia, Q. Li, Y. Li, Q. Chen, J. Li and D. He, Effect of rGO coating on interconnected Co_3O_4 nanosheets and improved supercapacitive behavior of Co_3O_4/rGO/NF architecture, *Nano-Micro Lett.*, 2017, **9**, 38.

41 J. Wang, D. Wang, Y. Chen, W. Wang, N. Mitsuzaki and Z. Chen, Activity engineering of cobalt-based oxide materials for high performance supercapacitors: from morphology regulation to structural optimization, Sustain, *Energy Fuels*, 2022, **6**, 5243–5255.

42 A. Shakoor, M. Adnan, M. Luqman, M. A. Khan, S. M. Ramay, F. Ahmad and S. Atiq, Synergistic improvements in ionic conductivity, diffusion dynamics, and transference numbers for $LaNiO_3$/MXene supercapacitor electrodes, *Batteries Supercaps*, 2025, e202500014.

43 K. Mallikarjuna, G. R. Reddy, M. A. Ghanem, G. R. Dillip and S. W. Joo, Insights of oxygen vacancies engineered structural, morphological, and electrochemical attributes of Cr-doped Co_3O_4 nanoparticles as redox active battery-type electrodes for hybrid supercapacitors, *J. Energy Storage*, 2024, **100**, 113751.

44 S. L. Jadhav, A. L. Jadhav, P. B. Sarawade, B. K. Mandlekar and A. V. Kadam, Mo-doped porous Co_3O_4 nanoflakes as an electrode with the enhanced capacitive contribution for asymmetric supercapacitor application, *J. Energy Storage*, 2024, **82**, 110540.

45 X. Mao, H. Liu, J. Xu, M. Li and W. Yang, Surface reconstruction of Co_3O_4/rGO heterointerface enabling high-performance asymmetric supercapacitors, *J. Energy Storage*, 2024, **102**, 114128.

46 G. Mummoorthi, P. Kamarajar, A. Jayaram, S. K. Easwaran and N. Mani, Strategic engineering of NiO/Co_3O_4/rGO hybrid composite as a cathode material to enhance the electrochemical performance of supercapattery devices, *J. Energy Storage*, 2024, **86**, 111037.

47 R. Kumar, R. Thangappan, F. Ran, S. Sambasivam, M. D. Albaqami and S. Mohammad, Enriched performance of practical device assisted asymmetric supercapacitor: NiO/Co_3O_4 intercalated with rGO nanocomposite electrodes, *J. Energy Storage*, 2024, **85**, 111075.

48 G. Li, M. Chen, Y. Ouyang, D. Yao, L. Lu, L. Wang, X. Xia, W. Lei, S.-M. Chen and D. Mandler, Manganese doped Co_3O_4 mesoporous nanoneedle array for long cycle-stable supercapacitors, *Appl. Surf. Sci.*, 2019, **469**, 941–950.

49 M. Irfan, F. Sarfraz, A. Tariq, U. Waqas, S. M. Ramay, F. Afzal and S. Atiq, Enhanced supercapacitor dynamics mediated by systematic incorporation of rGO in Mn_3O_4 matrix, *Diamond Relat. Mater.*, 2024, **144**, 110948.

50 G. Khan, M. Luqman, M. Mehak, M. U. Salman, A. Mahmood, W. Al-Masry, M. Nawaz and S. Atiq, Integration of carbon nanotubes/MXene into Co-doped Ni_9S_8 nanostructures for enhanced energy storage mediated via efficient diffusion dynamics in hybrid supercapacitors, *J. Power Sources*, 2025, **660**, 238568.

51 S. Fatima, H. Raza, A. Shakoor, F. Saeed, M. Luqman, M. S. Akhtar, S. M. Ramay, S. Sarwar and S. Atiq, Microstructural tailoring for enhanced response of carbon nanotube-filled $BiMnO_3$ electrodes, *Mater. Chem. Phys.*, 2025, 131198.

52 K. Si, Z. Wang, H. Zhang, X. Sun, J. Zong, X. Wang and X. Zhang, Green synthesis of SiO_x/C-TiO_2 with continuous conductive network towards enhancing lithium storage performance, *J. Energy Storage*, 2024, **104**, 114493.

53 S. Wang, R. Zhao, S. Yao, B. Li, R. Liu, L. Hu, A. Zhang, R. Yang, X. Liu and Z. Fu, Stretching the c-axis of the Mn_3O_4 lattice with broadened ion transfer channels for enhanced Na-ion storage, *J. Mater. Chem. A*, 2021, **9**, 23506–23514.

54 M. Shahzad, F. Ahmad, M. Ibraheem, A. Shakoor, S. M. Ramay, M. R. Raza and S. Atiq, Tuning diffusion coefficient, ionic conductivity, and transference number in rGO/$BaCoO_3$ electrode material for optimized supercapacitor energy storage, *RSC Adv.*, 2025, **15**, 6308–6323.

55 P. R. Sørensen and T. Jacobsen, Conductivity, charge transfer and transport number—an ac-investigation of the polymer electrolyte LiSCN-poly (ethyleneoxide), *Electrochim. Acta*, 1982, **27**, 1671–1675.

56 A. Shahzad, M. Saleem, A. Shakoor, F. Ahmad, S. Atiq, O. Munir, S. M. Bin Arif and N. Bano, Investigating electrochemical properties in CNT-modified MoS_2/Se composites for supercapacitor electrodes, *J. Power Sources*, 2025, **656**, 238067.